

1 Cryo-electron tomography of *C. elegans* mitochondria reveals how the ATP
2 synthase dimer interface shapes crista membranes

3

4 Emma Buzzard^{1,2}, Mathew McLaren^{1,2}, Piotr Bragoszewski³, Andrea Brancaccio^{4,5}, Holly Ford⁵, Bertram
5 Daum^{1,2}, Patricia Kuwabara⁵, Ian Collinson⁵ & Vicki A.M. Gold^{1,2,*}.

6 1 Living Systems Institute, University of Exeter, Exeter, UK.

7 2 Faculty of Health and Life Sciences, University of Exeter, Exeter, UK.

8 3 Nencki Institute of Experimental Biology, Polish Academy of Sciences, Warsaw, Poland.

9 4 Institute of Chemical Sciences and Technologies "Giulio Natta", Department of Chemical Sciences and
10 Materials Technologies, National Research Council (CNR), Rome, Italy.

11 5 School of Biochemistry, University of Bristol, BS8 1TD, UK.

12 *corresponding author: Vicki Gold; +44 (0)1392 727454; v.a.m.gold@exeter.ac.uk

13

14 **Classification:** Biological Sciences, Biochemistry

15 **Keywords:** Mitochondria, ATP synthase, Cryo-electron tomography, Sub-tomogram averaging, AlphaFold.

16

17 **Abstract**

18 Mitochondrial ATP synthases form rows of dimers, which induce membrane curvature to give cristae their
19 characteristic lamellar or tubular morphology. The angle formed between the central stalks of ATP synthase
20 dimers varies between species. Using cryo-electron tomography and sub-tomogram averaging, we
21 determined the structure of the ATP synthase dimer from the nematode worm *C. elegans*. We showed that
22 the angle formed by the ATP synthase dimer is different to previously determined structures. The
23 consequences of species-specific differences at the dimer interface were investigated by comparing
24 mitochondrial morphology between *C. elegans* and *S. cerevisiae*. We reveal that a larger ATP synthase
25 dimer angle in *C. elegans* is consequent with more lamellar (flatter) cristae compared to yeast. The
26 underlying cause of this difference was investigated by generating an atomic model of the *C. elegans* ATP
27 synthase dimer by homology modelling and comparing it to an existing *S. cerevisiae* structure. We reveal
28 extensions and rearrangements of *C. elegans* subunits that maintain the dimer interface. We propose that
29 increased dimer angles resulting in flatter cristae could provide an energetic advantage for species that
30 inhabit variable-oxygen environments.

31

32 **Significance Statement**

33 ATP synthase, the world's smallest rotary motor, generates the energy required for all living processes.
34 The universal formation of ATP synthase dimers in mitochondria induces membrane curvature and cristae
35 formation, generating the famously convoluted inner mitochondrial membrane that maximises ATP
36 production. Intriguingly, the angle between ATP synthase dimers varies between species. Here, we report
37 the discovery of a novel ATP synthase dimer angle in mitochondria from the nematode worm *C. elegans*,
38 identify a relationship between dimer angle and crista membrane morphology, and exploit AlphaFold
39 homology modelling to investigate associated structural changes. In summary, we have taken steps
40 towards understanding the importance of subunit composition at the ATP synthase dimer interface,
41 providing insights into the origins of this evolutionary divergence.

42 **Main Text**

43

44 **Introduction**

45 The F_1F_o ATP synthase is a molecular motor ubiquitous to all living organisms. This machine is required
46 for the essential conversion of an electrochemical gradient into the universal energy currency ATP (1). The
47 ATP synthase is composed of a catalytic F_1 head connected to a membrane-embedded F_o motor by a
48 central stalk; the entire assembly is visualised as a lollipop shape when examined by electron microscopy
49 (2, 3). The central stalk transmits the torque generated by rotation of F_o to the F_1 head, and a peripheral
50 stalk acts as an elastic spring, ensuring malleable coupling between F_1 and F_o (4). Mitochondrial ATP
51 synthases across species share the same complement of core subunits with varying nomenclature (Table
52 S1) (5, 6). Here, we use the *C. elegans* nomenclature, exceptions being use of the *S. cerevisiae* naming
53 system for subunits missing in worms. The F_1 head is comprised of α and β subunits, the central stalk of γ ,
54 δ and ϵ subunits, the peripheral stalk of b d, F_6 and oligomycin sensitivity conferral protein (OSCP) subunits,
55 and the F_o motor contains the c-ring and subunit a.

56

57 Mitochondrial ATP synthases are capable of assembling into dimers (7), of which there are 4 types (8):
58 Type I is present in both multicellular (9–11) and unicellular organisms (12) and types II-IV are present in
59 various unicellular organisms (13–18), reviewed in (8). When compared to type II-IV dimers, previously
60 studied type I dimers contain an additional set of subunits at the dimer interface: e, f, g, i/j, k and 8 (8).
61 Based on biochemical and imaging experiments, subunits e and g were shown to be essential for dimer
62 formation (7, 11, 19–21). Dimers of ATP synthase assemble into oligomeric rows (or ribbons) along the
63 curved ridges of crista membranes, observed by cryo-electron tomography (cryoET) (9, 11, 22). This
64 oligomerisation (formation of dimer rows) is mediated by an ancestral motif in subunits e and g (20, 21) with
65 assistance from subunit k (5, 23, 24). Formation of dimer rows is required for crista membrane curvature,
66 and thus maintenance of lamellar or tubular shaped cristae (11, 12). Deformation of cristae into balloon-
67 like structures was observed in *S. cerevisiae* after knockdown of interface subunits e or g (11) and in ageing
68 *P. anserina*, when dimers disassociated into monomers (12). Moreover, molecular simulations indicated

69 that ATP synthase dimers have an innate propensity to induce membrane curvature (25). This was
70 confirmed experimentally when dimers reconstituted into liposomes spontaneously self-assembled into
71 oligomeric rows to engender this curvature, maintaining identical dimer angles to those observed in whole
72 mitochondria (26).

73

74 *In situ* structures of type I ATP synthase dimers have been determined from native membranes (12, 25–
75 28). Mammals and fungi both display an average angle between the dimer heads of $\sim 86^\circ$ (27). Interestingly,
76 higher-resolution single particle analysis of the purified bovine ATP synthase dimer reveals that dimer
77 angles likely vary around this average (between 76° and 95°), depending on catalytic state (29). Further
78 atomic-detail structures of purified mitochondrial type I ATP synthase dimers have also been determined
79 from mammals (*Bos taurus* (23) and fungi (*S. cerevisiae* (30) and *Y. lipolytica* (22)). The structure and
80 organisation of ATP synthase dimers have thus been studied across a range of different species, yet our
81 knowledge of invertebrates is lacking. The free living nematode worm *C. elegans* is a well-established
82 model system for the study of invertebrate cell and developmental biology (31), including the role of
83 mitochondria in metabolism, health, disease and aging (32). To complement *in vivo* physiological studies,
84 intact mitochondria can be stably prepared (33, 34) for biochemical and structural analyses (35).
85 Interestingly, studies have shown that nematodes lack the dimer-specific subunits *i/j*, *k* (36) and *8* (37)
86 found in mammals and fungi (Table S1). Subunit 8 is encoded by one of two overlapping ATP synthase
87 genes on the mitochondrial genome (38). Proteins encoded on the mitochondrial genome are translated
88 from essential genes (39, 40); thus it follows that subunit 8 is likely to be essential for respiration in mammals
89 and fungi. The lack of dimer-specific subunits in *C. elegans* provides a unique opportunity to investigate
90 how certain subunits influence ATP synthase dimer angles and mitochondrial morphology.

91

92 In this study, we employed cryoET and sub-tomogram averaging to reveal the structure and organisation
93 of the *C. elegans* ATP synthase, revealing a novel average dimer angle of 105° . We compared mitochondria
94 from both *C. elegans* and *S. cerevisiae* to investigate the relationship between ATP synthase dimer angle
95 and crista morphology. Finally, we used AlphaFold (41) to predict how protein chains in the *C. elegans* ATP

96 synthase dimer are arranged. This allowed us to analyse changes at the dimer interface and postulate the
97 cause of differences in angle. We speculate that an evolutionary divergence at the dimer interface and
98 corresponding widening of the dimer angle may be an adaptation to more variable oxygen environments.

99

100 **Results**

101 **The architecture of the *C. elegans* ATP synthase dimer**

102 To determine the arrangement and architecture of ATP synthase dimers in *C. elegans*, tomograms of whole
103 mitochondria (Fig. 1A) and of isolated crista membranes (Fig. 1B) were analysed. ATP synthases were
104 unambiguously identified by the characteristic lollipop shape of the 10 nm diameter F₁ heads positioned
105 ~10 nm away from the membrane. We confirmed the presence of oligomeric ATP synthase dimer ribbons,
106 localised at the sharp curved ridges of crista membranes, in both samples (Fig. 1A, B). Due to the obscuring
107 presence of a dense matrix in whole mitochondria, many more dimers could be visualised in crista
108 membrane samples. Therefore, 3,234 dimer pairs were extracted from the crista membrane data for sub-
109 tomogram averaging. After classification, a map of the *C. elegans* ATP synthase dimer was determined
110 from 1,755 dimer pairs (Fig. 1C, Fig. S1, S2). Both the central and peripheral stalks were resolved clearly.

111

112 Previous studies have revealed a type I dimer angle of ~86° across a range of mammalian and fungal
113 species (12, 25–28). The architecture of the *C. elegans* ATP synthase dimer is unlike any other species
114 studied so far, with an average angle of 105° between the dimer heads (Fig. 2A). A comparison to a sub-
115 tomogram average of the *S. cerevisiae* dimer (42), revealed that the wider dimer angle in *C. elegans*
116 corresponds with a sharper angle of membrane curvature (50° compared to 74°) (Fig. 2B). Accordingly,
117 opposing sides of the *C. elegans* crista membranes are in closer proximity than in *S. cerevisiae* (16.5 nm
118 compared to 20 nm). Intriguingly, the dimer interface in the *C. elegans* map was visually remarkably
119 different to its *S. cerevisiae* counterpart (Fig. 2B), and indeed all other type I dimers studied to date (12,
120 25–28). This could be due to the different complement of dimer interface subunits present in *C. elegans*
121 compared to *S. cerevisiae* (Table S1, Fig. 2C). We also analysed the inter-dimer distance and angle

122 between dimer heads in consecutive dimers in the oligomeric rows. This revealed an inter-dimer distance
123 of 12.5 nm and angle between dimer heads of 20°. Despite differences in dimer angle, these values are
124 similar to those reported previously for the type II dimer from green algae (*Polytomella* sp.) (26) (Fig. S3),
125 suggesting that dimer angle does not influence oligomerisation of ATP synthases into rows.

126

127 **A wider dimer angle in *C. elegans* corresponds to flatter cristae**

128 We hypothesised that the wider dimer angle associated with sharper membrane curvature in the *C. elegans*
129 ATP synthase dimer (Fig. 2B) would produce flatter cristae with a larger surface area to volume ratio. To
130 test this, tomographic data of whole mitochondria from *C. elegans* and *S. cerevisiae* were collected and
131 quantified. Qualitatively, *C. elegans* mitochondria have more lamellar shaped (or flatter) cristae, with sharp
132 curved ridges, compared to mitochondria from *S. cerevisiae* (Fig. 3A, 3B, Movie S1 & S2). The surface
133 area and volume of the crista membranes were quantified, to reveal that the surface area to volume ratio
134 of the average crista membrane was significantly higher (~1.5 fold, **** $p \leq 0.0001$) in *C. elegans* than in
135 *S. cerevisiae* (Fig. 3C). In accordance with this, the average crista width in *C. elegans* (~10 nm) was half
136 the width of cristae in *S. cerevisiae* (~20 nm) (Fig. 3D, E and F). We speculated that narrower cristae in *C.*
137 *elegans* may allow more efficient membrane packing into the mitochondrial volume. However, no significant
138 difference was found between the total crista volume relative to mitochondrial volume between the two
139 organisms (Fig. 3G). In summary, this suggests that dimer angle exerts influence on mitochondrial
140 morphology at the level of membrane curvature, but this does not alter membrane packing.

141

142 Mitochondria are dynamic organelles, and crista morphology can be influenced by a wide range of factors
143 such as metabolic state (43–45). However, the average ATP synthase dimer angle remains consistent
144 when imaged in membranes or on purification in detergent (27, 29). To ensure that morphological
145 differences observed here in whole mitochondria were not a result of different preparation conditions, we
146 also measured the degree of membrane curvature in isolated cristae containing *C. elegans* and *S.*
147 *cerevisiae* ATP synthase dimers. Our results were consistent with the results obtained *in situ*, with a shorter

148 crista width observed for the *C. elegans* dimer average (Fig. 2B). This indicates that the dimer angle
149 remains consistent, regardless of how the sample was prepared or analysed.

150

151 **A unique arrangement of subunits at the *C. elegans* dimer interface**

152 We observed additional density at the *C. elegans* dimer interface (Fig. 2B), which has not been observed
153 in other type I structures determined to date (27). Nematodes are missing subunit 8 (37) (Table S1, Fig.
154 2C), which plays a key structural role in other species (22, 23, 30, 46) and is considered essential for
155 respiration (39, 40). Therefore, it is likely that considerable rearrangements at the dimer interface would
156 need to occur to account for the lack of subunit 8; this could contribute to the observed change of dimer
157 angle. To explore this possibility, we performed multisequence alignments with *C. elegans*, *S. cerevisiae*
158 and *B. taurus* (47–49). This revealed extensions in the 3 *C. elegans* subunits located at the dimer interface
159 (e, f and g), and in 3 of the 4 subunits in the peripheral stalk (b, d and F₆) (Fig. S4). Mass spectrometry was
160 used to confirm that the extensions identified by sequence in the dimer interface subunits are present in
161 the mature proteins (Fig. S5).

162

163 To position the dimer interface subunits in the *C. elegans* ATP synthase, we used AlphaFold (41) to predict
164 the structures of individual subunits and build a homology model. The mean pLDDT score (a per-residue
165 measure of local confidence on a scale from 0 – 100) of each AlphaFold prediction was > 70 (Table S2,
166 Fig. S6), and therefore defined as a “confident” prediction by the software. Structures of peripheral stalk
167 subunits b, d and F₆ were predicted together as a multimer (50), since individual predictions were not
168 reliable. The predicted structures were then fitted sequentially into a scaffold provided by the *S. cerevisiae*
169 ATP synthase dimer [PDB 6B8H] (Fig. S7, Fig. 4A). Extensions in key *C. elegans* dimer interface subunits
170 relative to their yeast homologues are clearly visible (Fig. S8). The *C. elegans* ATP synthase dimer was
171 then split into monomers and each was fitted sequentially into our sub-tomogram average dimer map (Fig.
172 S7, Fig. 4B), improving the fit considerably (Fig. S9). Our homology model correlated well to the sub-

173 tomogram averaging map (Fig. S10 and Table S3), allowing a comparison of *S. cerevisiae* and *C. elegans*
174 ATP synthase dimers (Fig. 4C).

175

176 Interestingly, the additional density identified in our sub-tomogram averaging map at the dimer interface
177 (Fig. 2B) appears to now be filled by a rearrangement of the extended subunits f and g (Fig. 4C, D & E). In
178 addition, extensions at the base of the peripheral stalk (subunits b, d and F₆) also appear to contribute to
179 the greater mass at the *C. elegans* dimer interface compared to *S. cerevisiae* (Fig. S11). Despite this, there
180 are unfilled gaps at the dimer interface. It is plausible that specific lipids could also contribute to the mass
181 observed, which is in line with their identification and role in stabilisation of the dimer interface (23, 51). We
182 also cannot exclude the possibility that there are additional subunits as yet unidentified in *C. elegans*.

183 Finally, we fitted the *C. elegans* ATP synthase dimer model into a row of oligomeric dimer pairs along the
184 curved edge of a crista (Fig. 4F, H). This reveals extensive inter-dimer interactions mediated by subunits e
185 and g (Fig. 4G, I and Fig. S12), in agreement with recent work demonstrating the key role that these
186 subunits play a role in oligomerisation / row formation (21).

187

188 **Discussion**

189 Owing to the essential and universal role of the ATP synthase across eukaryotic species, it is remarkable
190 that the dimeric arrangement can be so variable (10). Until now, the arrangement of ATP synthases in
191 invertebrates was unknown, as was the correlation between dimer angle and whole mitochondrial
192 morphology. In this work, a novel dimer angle for the ATP synthase from the nematode worm *C. elegans*
193 was discovered. By comparing worm and yeast mitochondria, we discovered that a wider ATP synthase
194 dimer angle was associated with a flatter crista membrane morphology. Since dimer row formation is known
195 to be instrumental in formation of curved ridges in crista membranes (11, 12, 26), it is consequent that
196 dimer angle influences the extent of membrane curvature.

197

198 AlphaFold is able to predict protein structures with high precision (41). Our homology model of the *C.*
199 *elegans* ATP synthase dimer thus allowed us to postulate how alterations in the organisation of subunits
200 could influence dimer architecture. The ATP synthase structure is relatively well conserved across species
201 (52), but more weakly at the dimer interface and peripheral stalk (53). In accordance with this, extensions
202 in 3 *C. elegans* subunits (e, f and g) result in the rearrangement of subunits at the dimer interface relative
203 to *S. cerevisiae*. In addition, changes are detected in peripheral stalk components, with a significant N-
204 terminal extension in subunit b, and a range of more subtle gaps and insertions in subunits d and F₆, which
205 bulk out the width of the dimer interface. Some dimer interface subunits present in *S. cerevisiae* (j, k and
206 8) are absent in *C. elegans*. Whilst it cannot be completely excluded that an as yet unidentified subunit may
207 substitute for 8, we speculate that the absence of 8 in worms (37) highlights an interesting evolutionary
208 divergence. Subunit 8 is usually encoded on the mitochondrial genome, indicating that it is essential (39,
209 40). Additionally, 8 appears to have a key structural role in joining the dimer interface to the peripheral stalk
210 (22, 23, 30, 46). It is therefore likely that the space vacated by the missing subunit 8 is either resolved by
211 the re-arrangement of neighbouring subunits, or substituted by one of the extensions of the F_O subunits
212 close by (b, d, e, f or g).

213

214 Mitochondria have evolved their highly convoluted crista membranes to increase their surface area (54),
215 hence accommodating the maximum amount of respiratory chain complexes. This has made it possible for
216 eukaryotic organisms to deal with higher energy demands than prokaryotes (54). However, we found that
217 the flatter cristae in *C. elegans* relative to *S. cerevisiae* is not associated with more efficient cristae
218 membrane packing into the mitochondrial volume. ATP synthesis is driven by the proton-motive force (PMF)
219 and the efficiency of ATP production is directly proportional to the local proton concentration. It has been
220 suggested that cristae serve as proton concentrators that facilitate a directed flow from the source
221 (respiratory chain) to sink (ATP synthase) (9, 27). On this premise, the concentration effect exerted by the
222 cristae would be directly proportional to the number of protons pumped in a given time and the volume of
223 the crista lumen. It follows that in a flatter crista of equivalent volume to a wider one (e.g. *C. elegans*
224 compared to *S. cerevisiae*), fewer protons would need to be pumped to reach a given concentration, and

225 hence to reach the PMF required to drive the ATP synthase. In addition, protons have been proposed to
226 preferably migrate from source to sink along membrane surfaces. If this is the case, then reducing the width
227 of the crista space will reduce the solvent volume that the protons can dissipate into, facilitating the
228 efficiency of ATP synthesis. Both of these factors could allow *C. elegans* to maximise energy production in
229 its soil-based habitat (55), where conditions range from near hypoxia to atmospheric (56, 57). Thus, we
230 propose that a wider ATP synthase dimer angle associated with flatter cristae may be paramount for
231 capitalising on ATP production when a higher level of oxygen becomes available, and that a range of angles
232 have evolved to meet the energetic needs of different organisms. Future studies geared towards
233 investigating dimer subunit composition, angle and corresponding crista morphology in a range of species
234 inhabiting different environments will be key. The divergence in ATP synthase dimer architecture relative
235 to yeast and mammalian systems makes *C. elegans* an ideal model system for further investigation of the
236 role of dimer angle in mitochondrial physiology, health and disease.

237

238 **Conclusions**

239 In this work, we discovered that the *C. elegans* mitochondrial ATP synthase forms a novel dimer interface
240 with an angle between subunits of 105°. We have shown that this unusually wide angle is associated with
241 flatter cristae compared with the yeast *S. cerevisiae*. We conclude that rearrangement of subunits at the
242 dimer interface controls dimer angle and accordingly the extent of membrane curvature. Since an energetic
243 advantage is likely to be proffered by an increased local proton concentration, we speculate that a range of
244 dimer angles may have evolved to alter crista diameter and thus suit bespoke energetic needs.

245 **Materials and Methods**

246

247 All standard reagents were purchased from Sigma-Aldrich (Burlington, USA).

248

249 ***C. elegans* and *S. cerevisiae* culture**

250 The *C. elegans* N2 Bristol strain was maintained at 20°C on 60 mm Nematode Growth Medium (NGM)
251 plates seeded with *E. coli* OP50. For large scale preparations, a semi-synchronised population of *C.*
252 *elegans* (achieved by starving so that they entered the dauer stage) (58, 59) were grown in a liquid
253 suspension of *E. coli* NA22 in S-basal complete medium (60) at 20°C, shaking at 200 rpm for 3 days to
254 achieve adults. For further details see (34). *S. cerevisiae* 'Bakers's yeast' S288C derivative strains YPH499
255 were cultured at 19 - 24°C in YPGal or YPG medium (1% w/v yeast extract, 2% w/v bactopectone, 2% w/v
256 galactose or 3% w/v glycerol) until OD 2-2.5 was reached. For further details see (61).

257

258 **Mitochondrial isolation**

259 *C. elegans* and *S. cerevisiae* were both harvested from liquid cultures by low speed centrifugation. *C.*
260 *elegans* preparation required an additional sucrose flotation step to remove debris. To soften the *C. elegans*
261 cuticle, the pellets underwent collagenase treatment (1 U/ml collagenase, 100 mM Tris-HCl pH 7.4 and 1
262 mM CaCl₂), whilst *S. cerevisiae* pellets underwent dithiothreitol (10 mM DTT, 100 mM Tris-SO₄ pH 9.4)
263 and zymolyase treatment (4.5mg/g zymolyase, 1.2 M sorbitol, 20 mM potassium phosphate, pH 7.4) to
264 disrupt the cell wall. Pellets from both species were re-suspended in homogenisation buffers. For *C.*
265 *elegans*, this was STEG/M (220 mM mannitol, 70 mM sucrose, 5 mM Tris-HCl pH 7.4 and 1 mM EGTA
266 supplemented with 1 mM PMSF in methanol and 1% (w/v) fatty acid-free BSA). For *S. cerevisiae* the
267 homogenization buffer contained 0.6 M sorbitol, 10 mM Tris-HCl pH 7.4, 1 mM PMSF, 0.2% (w/v) BSA, 2
268 mM magnesium acetate. The re-suspended *C. elegans* or *S. cerevisiae* samples were homogenised in a
269 glass-Teflon Potter homogeniser to break open cells. Both samples were subsequently spun at low speed
270 (750 – 3000 x g for 5-15 minutes) to remove cell debris and nuclei, and then at higher speed (12,000 x g
271 for 15 minutes) to pellet mitochondria. Purified mitochondria were re-suspended in buffers that were

272 optimised to maintain intact mitochondria: 220 mM mannitol, 70 mM sucrose, 5 mM Tris-HCl pH 7.4 and 1
273 mM EGTA for *C. elegans* or 250 mM sucrose, 2 mM magnesium acetate, 10 mM Mops, pH 7.2 for *S.*
274 *cerevisiae*.

275

276 **Mitochondrial crista membrane isolation**

277 Crista membranes used for the sub-tomogram averaging experiments were generated by successive
278 freeze-thaw cycles of mitochondria at -80°C. To purify mitochondrial membranes from other cellular
279 material, membrane extracts were incubated for 1h at 4°C with an anti-NDUFS3 primary antibody
280 (ab14711; abcam) against the matrix arm of complex I from *C. elegans*, followed by a 3h incubation with
281 an anti-mouse secondary conjugated to a quantum dot emitting at 625 nm (Q22085; Invitrogen). Crista
282 membranes were separated from unbound antibodies and other cellular material on an Optiprep gradient
283 with 10 layers (200 µl volume each) ranging from 0 to 27% v/v of iodixanol in STEG/M buffer, by
284 centrifugation at 80,000 x g for 30 min at 4°C using a TLS-55 rotor (Beckman Coulter Inc., Miami, FL, USA).
285 Crista membranes were identified and removed based on fluorescence under a UV lamp. Samples were
286 then diluted in STEG/M buffer to wash out the iodixanol, and spun at 20,000 x g for 15 min at 4 °C to pellet
287 the membranes. The enriched cristae were again re-suspended in STEG/M buffer.

288

289 **Electron cryo-tomography**

290 Whole mitochondria or crista membranes were mixed 1:1 with 10 nm gold fiducials (Aurion, Wageningen,
291 The Netherlands), applied to glow-discharged holey carbon EM grids (Quantifoil, Jena, Germany), and
292 blotted for 5-6 seconds, followed by plunge-freezing in liquid ethane using a Vitrobot Mark IV
293 (ThermoFisher, Massachusetts, USA) for *C. elegans*, or a home-made device for whole *S. cerevisiae*
294 mitochondria. Pre-screening of *C. elegans* grids was carried out using an FEI Tecnai Spirit 120kV
295 microscope (ThermoFisher), with a Oneview CCD Camera (Gatan, Pleasanton, USA). CryoET was
296 performed using the same microscope for whole mitochondria, or using a 200 kV Talos Arctica
297 (ThermoFisher) for crista membranes, equipped with a K2 direct electron detector camera and a GIF

298 Quantum LS energy filter (Gatan). CryoET of whole *S. cerevisiae* mitochondria was performed using a 300
299 kV Titan Krios (ThermoFisher), K2 direct electron detector camera and a GIF Quantum LS energy filter
300 (Gatan). Single tilt image series' (± 60 , step size $1.5^\circ - 2^\circ$) were collected at -5 to $-8 \mu\text{m}$ underfocus at
301 nominal magnification of 21,000 x for whole mitochondria and 39,000 x for crista membranes,
302 corresponding to 5.4 and 3.58 Å pixel sizes respectively for *C. elegans*, or 26,000 x for whole mitochondria
303 from *S. cerevisiae*, corresponding to a 4.51 Å pixel size. The total dose per tomogram was $\sim 120 \text{ e}^-/\text{Å}^2$ for
304 whole mitochondria, and $\sim 80 \text{ e}^-/\text{Å}^2$ for isolated cristae. Tomograms were aligned using the gold fiducials in
305 IMOD (University of Colorado, United States) (62) and volumes reconstructed via weighted back-projection.
306 Contrast was enhanced by nonlinear anisotropic diffusion (NAD) filtering (63), followed by manual
307 segmentation, also in IMOD. ImageJ (64) was used to generate movies of segmentations generated in
308 IMOD.

309

310 **Subtomogram averaging**

311 3,234 *C. elegans* ATP synthase dimers were picked manually in IMOD, using NAD-filtered tomograms.
312 Subvolumes containing the ATP synthase dimer were then extracted from tomograms that had not been
313 NAD filtered. These sub-volumes were CTF corrected and imported into Relion 3.1 (65) using the approach
314 and script described in (66). A reference-free initial model was generated using 3 x binned subvolumes and
315 2,481 dimers were selected by 2D classification for an unbinned refinement. Finally, 1,755 dimers were
316 selected from a 3D classification of this refined model to enter a final round of refinement and post-
317 processing, resulting in a 38.6 Å resolution map. Fig. S1 details the full workflow.

318

319 **Homology model generation**

320 AlphaFold was used to predict five structural models of each ATP synthase subunit in *C. elegans* based on
321 their mature protein sequence (41). Mature sequences were determined using MitoFates (67) or TargetP-
322 2.0 (68) to predict mitochondrial targeting sequences. All ATP synthase subunits known to be present in *C.*
323 *elegans* were included, excepting a putative homologue of subunit j, on account of its poor alignment with

324 other homologues, and absence of any corresponding peptides in mass spectrometry analysis of the *C.*
325 *elegans* dimer. The structures of peripheral stalk subunits b, d and F₆ were predicted using AlphaFold
326 multimer (50), as the individual predictions were unreliable. The models for each subunit with the highest
327 average pLDDT score were fitted sequentially to a scaffold provided by the atomic model of the *S.*
328 *cerevisiae* ATP synthase dimer [PDB 6BH8] in ChimeraX (69) using the Matchmaker tool. Where a subunit
329 had more than one isoform, the version with the highest pLDDT score was used. In the case of subunit b,
330 the isoform with the highest pLDDT score is also the only isoform expressed in somatic tissues (70). The
331 resulting structure was divided into monomers, and fitted sequentially into the sub-tomogram average of
332 the *C. elegans* ATP synthase dimer using the “fit in volume” tool in ChimeraX. The workflow is shown in
333 Fig. S7. The resulting homology model was converted into an MRC map using the pdb2mrc command in
334 EMAN2 (71). This map could then be fitted to the sub-tomogram average map of the *C. elegans* dimer for
335 comparison (Fig. S10). The yeast monomeric atomic model [PDB 6CP6] (72) was used for additional
336 analysis in Fig. S8.

337

338 **Mass spectrometry**

339 The ATP synthase was purified from *C. elegans* mitochondria using a method described previously (73,
340 74), and analysed by Nano-LC mass spectrometry. Briefly, isolated mitochondria were solubilised and
341 mixed with a His-tagged inhibitor protein IF₁. This suspension was applied to a Nickel column to capture
342 inhibited ATP synthase. The fraction most enriched in ATP synthase subunits was taken for mass
343 spectrometry analysis. Further details are given in Supporting Information.

344 **References**

- 345 1. P. Mitchell, Chemiosmotic coupling in oxidative and photosynthetic phosphorylation. *Biol. Rev.* **41**,
346 445–502 (1966).
- 347 2. J. L. Rubinstein, Structure of the mitochondrial ATP synthase by electron cryomicroscopy. *EMBO*
348 *J.* **22**, 6182–6192 (2003).
- 349 3. W. C. Y. Lau, L. A. Baker, J. L. Rubinstein, Cryo-EM structure of the yeast ATP synthase. *J. Mol.*
350 *Biol.* **382**, 1256–1264 (2008).
- 351 4. M. Sobti, *et al.*, Cryo-EM structures of the autoinhibited *E. coli* ATP synthase in three rotational
352 states. *Elife* **5**, e21598 (2016).
- 353 5. J. He, *et al.*, Assembly of the membrane domain of ATP synthase in human mitochondria. *Proc.*
354 *Natl. Acad. Sci. USA.* **115**, 2988–2993 (2018).
- 355 6. J. Song, N. Pfanner, T. Becker, Assembling the mitochondrial ATP synthase. *Proc. Natl. Acad.*
356 *Sci. USA.* **115**, 2850–2852 (2018).
- 357 7. I. Arnold *et al.*, Yeast mitochondrial F_1F_0 -ATP synthase exists as a dimer: identification of three
358 dimer-specific subunits. *EMBO J.* **17**, 7170–7178 (1998).
- 359 8. W. Kühlbrandt, Structure and mechanisms of F-Type ATP synthases. *Annu. Rev. Biochem.* **88**,
360 515–549 (2019).
- 361 9. M. Strauss, G. Hofhaus, R. R. Schröder, W. Kühlbrandt, Dimer ribbons of ATP synthase shape the
362 inner mitochondrial membrane. *EMBO J.* **27**, 1154–1160 (2008).
- 363 10. K. M. Davies, *et al.*, Macromolecular organization of ATP synthase and complex I in whole
364 mitochondria. *Proc. Natl. Acad. Sci. USA.* **108**, 14121–14126 (2011).
- 365 11. K. M. Davies, C. Anselmi, I. Wittig, J. D. Faraldo-Gómez, W. Kühlbrandt, Structure of the yeast F_1
366 F_0 -ATP synthase dimer and its role in shaping the mitochondrial cristae. *Proc. Natl. Acad. Sci.*
367 *USA.* **109**, 13602–13607 (2012).
- 368 12. B. Daum, A. Walter, A. Horst, H. D. Osiewacz, W. Kühlbrandt, Age-dependent dissociation of ATP

- 369 synthase dimers and loss of inner-membrane cristae in mitochondria. *Proc. Natl. Acad. Sci. USA*.
370 **110**, 15301–15306 (2013).
- 371 13. M. Vázquez-Acevedo, *et al.*, Dissecting the peripheral stalk of the mitochondrial ATP synthase of
372 chlorophycean algae. *Biochim. Biophys. Acta - Bioenerg.* **1857**, 1183–1190 (2016).
- 373 14. A. W. Mühleip, *et al.*, Helical arrays of U-shaped ATP synthase dimers form tubular cristae in
374 ciliate mitochondria. *Proc. Natl. Acad. Sci. USA*. **113**, 8442–8447 (2016).
- 375 15. A. W. Mühleip, C. E. Dewar, A. Schnauffer, W. Kühlbrandt, K. M. Davies, *In situ* structure of
376 trypanosomal ATP synthase dimer reveals a unique arrangement of catalytic subunits. *Proc. Natl.*
377 *Acad. Sci. USA*. **114**, 992–997 (2017).
- 378 16. M. G. Montgomery, O. Gahura, A. G. W. Leslie, A. Zíková, J. E. Walker, ATP synthase from
379 *Trypanosoma brucei* has an elaborated canonical F₁-domain and conventional catalytic sites.
380 *Proc. Natl. Acad. Sci. USA*. **115**, 2102–2107 (2018).
- 381 17. K. M. Davies, W. Kühlbrandt, Structure of the catalytic F₁ head of the F₁-F_o ATP synthase from
382 *Trypanosoma brucei*. *Proc. Natl. Acad. Sci. USA*. **115**, E2906–E2907 (2018).
- 383 18. B. J. Murphy, *et al.*, Rotary substates of mitochondrial ATP synthase reveal the basis of flexible
384 F₁-F_o coupling. *Science*. **364**, 6446(2019).
- 385 19. I. Arnold *et al.*, ATP Synthase of yeast mitochondria. Isolation of subunit j and disruption of the
386 ATP18 gene. *J. Biol. Chem.* **274**, 36–40 (1999).
- 387 20. P. Paumard, *et al.*, The ATP synthase is involved in generating mitochondrial cristae morphology.
388 *EMBO J.* **21**, 221–230 (2002).
- 389 21. O. Gahura, *et al.*, An ancestral interaction module promotes oligomerization in divergent
390 mitochondrial ATP synthases. *Nat. Commun.* **13**, 5989 (2022).
- 391 22. A. Hahn, *et al.*, Structure of a complete ATP synthase dimer reveals the molecular basis of inner
392 mitochondrial membrane morphology. *Mol. Cell* **63**, 445–456 (2016).
- 393 23. T. E. Spikes, M. G. Montgomery, J. E. Walker, Structure of the dimeric ATP synthase from bovine

- 394 mitochondria. *Proc. Natl. Acad. Sci. USA*. **117**, 23519–23526 (2020).
- 395 24. J. He, *et al.*, Assembly of the peripheral stalk of ATP synthase in human mitochondria. *Proc. Natl.*
396 *Acad. Sci. USA*. **117**, 29602–29608 (2020).
- 397 25. C. Anselmi, K. M. Davies, J. D. Faraldo-Gómez, Mitochondrial ATP synthase dimers
398 spontaneously associate due to a long-range membrane-induced force. *J. Gen. Physiol.* **150**,
399 763–770 (2018).
- 400 26. T. B. Blum, A. Hahn, T. Meier, K. M. Davies, W. Kühlbrandt, Dimers of mitochondrial ATP
401 synthase induce membrane curvature and self-assemble into rows. *Proc. Natl. Acad. Sci. USA*.
402 **116**, 4250–4255 (2019).
- 403 27. K. M. Davies, *et al.*, Macromolecular organization of ATP synthase and complex I in whole
404 mitochondria. *Proc. Natl. Acad. Sci. USA*. **108**, 14121–14126 (2011).
- 405 28. W. Kühlbrandt, Structure and function of mitochondrial membrane protein complexes. *BMC Biol.*
406 **13**, 89 (2015).
- 407 29. T. E. Spikes, M. G. Montgomery, J. E. Walker, Interface mobility between monomers in dimeric
408 bovine ATP synthase participates in the ultrastructure of inner mitochondrial membranes. *Proc.*
409 *Natl. Acad. Sci. USA*. **118**, 8 (2021).
- 410 30. H. Guo, S. A. Bueler, J. L. Rubinstein, Atomic model for the dimeric F_o region of mitochondrial
411 ATP synthase. *Science*. **358**, 936–940 (2017).
- 412 31. M. Markaki, N. Tavernarakis, Modeling human diseases in *Caenorhabditis elegans*. *Biotechnol. J.*
413 **5**, 1261–1276 (2010).
- 414 32. K. Yasuda, *et al.*, Age-related changes of mitochondrial structure and function in *Caenorhabditis*
415 *elegans*. *Mech. Ageing Dev.* **127**, 763–770 (2006).
- 416 33. L. I. Grad, L. C. Sayles, B. D. Lemire, Isolation and functional analysis of mitochondria from the
417 nematode *Caenorhabditis elegans*. *Methods Mol. Biol.* **272**, 51-66 (2007).
- 418 34. A. Knapp-Wilson, *et al.*, Maintenance of complex I and its supercomplexes by NDUF-11 is

- 419 essential for mitochondrial structure, function and health. *J. Cell Sci.* **134**, jcs258399 (2021).
- 420 35. R. R. Murfitt, K. Vogel, D. R. Sanadi, Characterization of the mitochondria of the free-living
421 nematode, *Caenorhabditis elegans*. *Comp. Biochem. Physiol. Part B Comp. Biochem.* **53B**, 423–
422 430 (1976).
- 423 36. W. Y. Tsang, B. D. Lemire, The role of mitochondria in the life of the nematode, *Caenorhabditis*
424 *elegans*. *Biochim. Biophys. Acta - Mol. Basis Dis.* **1638**, 91–105 (2003).
- 425 37. R. Okimoto, J. L. Macfarlane, D. O. Clary, D. R. Wolstenholme, The mitochondrial genomes of two
426 nematodes, *Caenorhabditis elegans* and *Ascaris suum*. *Genetics* **130**, 471–498 (1992).
- 427 38. I. M. Fearnley, J. E. Walker, Two overlapping genes in bovine mitochondrial DNA encode
428 membrane components of ATP synthase. *EMBO J.* **5**, 2003–2008 (1986).
- 429 39. J. Shen, *et al.*, Oxygen consumption rates and oxygen concentration in Molt-4 cells and their
430 mtDNA Depleted ($\rho 0$) Mutants. *Biophys. J.* **84**, 1291–1298 (2003).
- 431 40. J. A. Stuart, M. F. Brown, Mitochondrial DNA maintenance and bioenergetics. *Biochim. Biophys.*
432 *Acta - Bioenerg.* **1757**, 79–89 (2006).
- 433 41. J. Jumper, *et al.*, Highly accurate protein structure prediction with AlphaFold. *Nature* **596**, 583–589
434 (2021).
- 435 42. K. M. Davies, *et al.*, Visualization of ATP synthase dimers in mitochondria by electron cryo-
436 tomography. *J. Vis. Exp.*, e51228 (2014).
- 437 43. C. A. Mannella, Structure and dynamics of the mitochondrial inner membrane cristae. *Biochim.*
438 *Biophys. Acta - Mol. Cell Res.* **1763**, 542–548 (2006).
- 439 44. G. C. Pereira, *et al.*, Hexokinase II dissociation alone cannot account for changes in heart
440 mitochondrial function, morphology and sensitivity to permeability transition pore opening following
441 ischemia. *PLoS One* **15**, e0234653 (2020).
- 442 45. C. R. Hackenbrock, Ultrastructural bases for metabolically linked mechanical activity in
443 mitochondria I. Reversible ultrastructural changes with change in metabolic steady state in

- 444 isolated liver mitochondria. *J. Cell Biol.* **30**, 269–297 (1966).
- 445 46. J. Gu, *et al.*, Cryo-EM structure of the mammalian ATP synthase tetramer bound with inhibitory
446 protein IF1. *Science*. **364**, 1068–1075 (2019).
- 447 47. F. Sievers, *et al.*, Fast, scalable generation of high-quality protein multiple sequence alignments
448 using Clustal Omega. *Mol. Syst. Biol.* **7**, 539 (2011).
- 449 48. M. Goujon, *et al.*, A new bioinformatics analysis tools framework at EMBL-EBI. *Nucleic Acids Res.*
450 **38**, W695–W699 (2010).
- 451 49. H. McWilliam, *et al.*, Analysis Tool Web Services from the EMBL-EBI. *Nucleic Acids Res.* **41**,
452 W597–W600 (2013).
- 453 50. R. Evans, *et al.*, Protein complex prediction with AlphaFold-Multimer. *bioRxiv* (2021)
454 <https://doi.org/10.1101/2021.10.04.463034> (November 30, 2021).
- 455 51. A. Mühleip, S. E. McComas, A. Amunts, Structure of a mitochondrial ATP synthase with bound
456 native cardiolipin. *Elife* **8**, e51179 (2019).
- 457 52. M. Yoshida, E. Muneyuki, T. Hisabori, ATP synthase - a marvellous rotary engine of the cell. *Nat.*
458 *Rev. Mol. Cell Biol.* **2**, 669–677 (2001).
- 459 53. G. M. Courbon, J. L. Rubinstein, CryoEM reveals the complexity and diversity of ATP synthases.
460 *Front. Microbiol.* **13**, 864006 (2022).
- 461 54. N. Lane, W. Martin, The energetics of genome complexity. *Nature* **467**, 929–934 (2010).
- 462 55. E. Moreno, A. McGaughran, C. Rödelsperger, M. Zimmer, R. J. Sommer, Oxygen-induced social
463 behaviours in *Pristionchus pacificus* have a distinct evolutionary history and genetic regulation
464 from *Caenorhabditis elegans*. *Proc. R. Soc. B Biol. Sci.* **283**, 20152263 (2016).
- 465 56. K. H. Tan, *Principles of soil chemistry*, 4th Ed. (2011)
- 466 57. W. Wang, *et al.*, Effect of oxygen concentration on the composting process and M
467 maturity. *Compost Sci. Util.* **15**, 184–190 (2007).

- 468 58. N. Fielenbach, A. Antebi, *C. elegans* dauer formation and the molecular basis of plasticity. *Genes*
469 *Dev.* **22**, 2149–2165 (2008).
- 470 59. Karp X. Working with dauer larvae. (August 9, 2018), *WormBook*, ed. The *C. elegans* Research
471 Community, WormBook, doi/10.1895/wormbook.1.180.1, <http://www.wormbook.org>
- 472 60. Stiernagle, T. Maintenance of *C. elegans* (February 11, 2006), *WormBook*, ed. The *C. elegans*
473 Research Community, WormBook, doi/10.1895/wormbook.1.101.1, <http://www.wormbook.org>
- 474 61. V. A. Gold, P. Chroscicki, P. Bragoszewski, A. Chacinska, Visualization of cytosolic ribosomes on
475 the surface of mitochondria by electron cryo-tomography. *EMBO Rep.* **18**, 1786–1800 (2017).
- 476 62. J. R. Kremer, D. N. Mastronarde, J. R. McIntosh, Computer visualization of three-dimensional
477 image data using IMOD. *J. Struct. Biol.* **116**, 71–76 (1996).
- 478 63. A. S. Frangakis, R. Hegerl, Noise reduction in electron tomographic reconstructions using
479 nonlinear anisotropic diffusion. *J. Struct. Biol.* **135**, 239–250 (2001).
- 480 64. C. A. Schneider, W. S. Rasband, K. W. Eliceiri, NIH Image to ImageJ: 25 years of image analysis.
481 *Nat. Methods* **9**, 671–675 (2012).
- 482 65. S. H. W. Scheres, Amyloid structure determination in RELION -3.1. *Acta Crystallogr. Sect. D*
483 *Struct. Biol.* **76**, 94–101 (2020).
- 484 66. T. A. M. Bharat, S. H. W. Scheres, Resolving macromolecular structures from electron cryo-
485 tomography data using subtomogram averaging in RELION. *Nat. Protoc.* **11**, 2054–2065 (2016).
- 486 67. Y. Fukasawa, *et al.*, MitoFates: Improved prediction of mitochondrial targeting sequences and their
487 cleavage sites. *Mol. Cell. Proteomics* **14**, 1113–1126 (2015).
- 488 68. J. J. A. Armenteros, *et al.*, Detecting sequence signals in targeting peptides using deep learning.
489 *Life Sci. Alliance* **2**, e201900429 (2019).
- 490 69. E. F. Pettersen, *et al.*, UCSF ChimeraX: Structure visualization for researchers, educators, and
491 developers. *Protein Sci.* **30**, 70–82 (2021).
- 492 70. I. Kawasaki, *et al.*, ASB-1, a germline-specific isoform of mitochondrial ATP synthase b subunit, is

- 493 required to maintain the rate of germline development in *Caenorhabditis elegans*. *Mech. Dev.* **124**,
494 237–251 (2007).
- 495 71. G. Tang, *et al.*, EMAN2: An extensible image processing suite for electron microscopy. *J. Struct.*
496 *Biol.* **157**, 38–46 (2007).
- 497 72. A. P. Srivastava, *et al.*, High-resolution cryo-EM analysis of the yeast ATP synthase in a lipid
498 membrane. *Science*. **360**, eaas9699 (2018).
- 499 73. T. E. Spikes, Structural studies of the mitochondrial F-ATPase (doctoral thesis). University of
500 Cambridge. (2017) <https://doi.org/10.17863/CAM.21471> (December 7, 2022).
- 501 74. M. J. Runswick, *et al.*, The affinity purification and characterization of ATP synthase complexes
502 from mitochondria. *Open Biol.* **3** (2012).
- 503

504 **Data availability**

505

506 The sub-tomogram averaging maps generated in this study have been deposited in the Electron Microscopy
507 Data Bank (EMDB) under accession code EMD-16216. The source image data have been deposited to the
508 Electron Microscopy Public Image Archive (EMPIAR) under accession number [currently unknown].

509

510 **Acknowledgments**

511

512 We thank Rebekah White in the lab of Cameron Weadick for sharing equipment, resources and knowledge
513 for nematode maintenance. We acknowledge Werner Kühlbrandt at the Max-Planck Institute of Biophysics,
514 Frankfurt, Germany, where the *S. cerevisiae* data were collected. We thank Agnieszka Chacinska at IMol
515 Polish Academy of Sciences, Warsaw, Poland, for supporting the *S. cerevisiae* based experiments. We
516 acknowledge access and support of the GW4 Facility for High-Resolution Electron Cryo-Microscopy,
517 funded by the Wellcome Trust (202904/Z/16/Z and 206181/Z/17/Z) and BBSRC (BB/R000484/1), and are
518 grateful to Ufuk Borucu of the GW4 Regional Facility for High-Resolution Electron Cryo-Microscopy for help
519 with screening and data collection. We thank Kate Heesom from the Bristol Proteomics Facility for collecting
520 and analysing mass spectrometry data. EB was supported by the Biotechnology and Biological Sciences
521 Research Council-funded South West Biosciences Doctoral Training Partnership [DTP2: BB/M009122/1]
522 awarded to VG. MM was supported by a BBSRC responsive mode grant (BB/R008639/1) grant awarded
523 to VG. BD received funding from the European Research Council (ERC) under the European Union's
524 Horizon 2020 research and innovation programme (grant agreement No 803894). This work was also
525 funded by the Wellcome Trust (a Wellcome Investigator award (104632) to IC, which supported HF. The
526 funders had no role in study design, data collection and interpretation, or the decision to submit the work
527 for publication. For the purpose of Open Access, the authors have applied a CC BY public copyright license
528 to any Author Accepted Manuscript version arising from this submission.

529

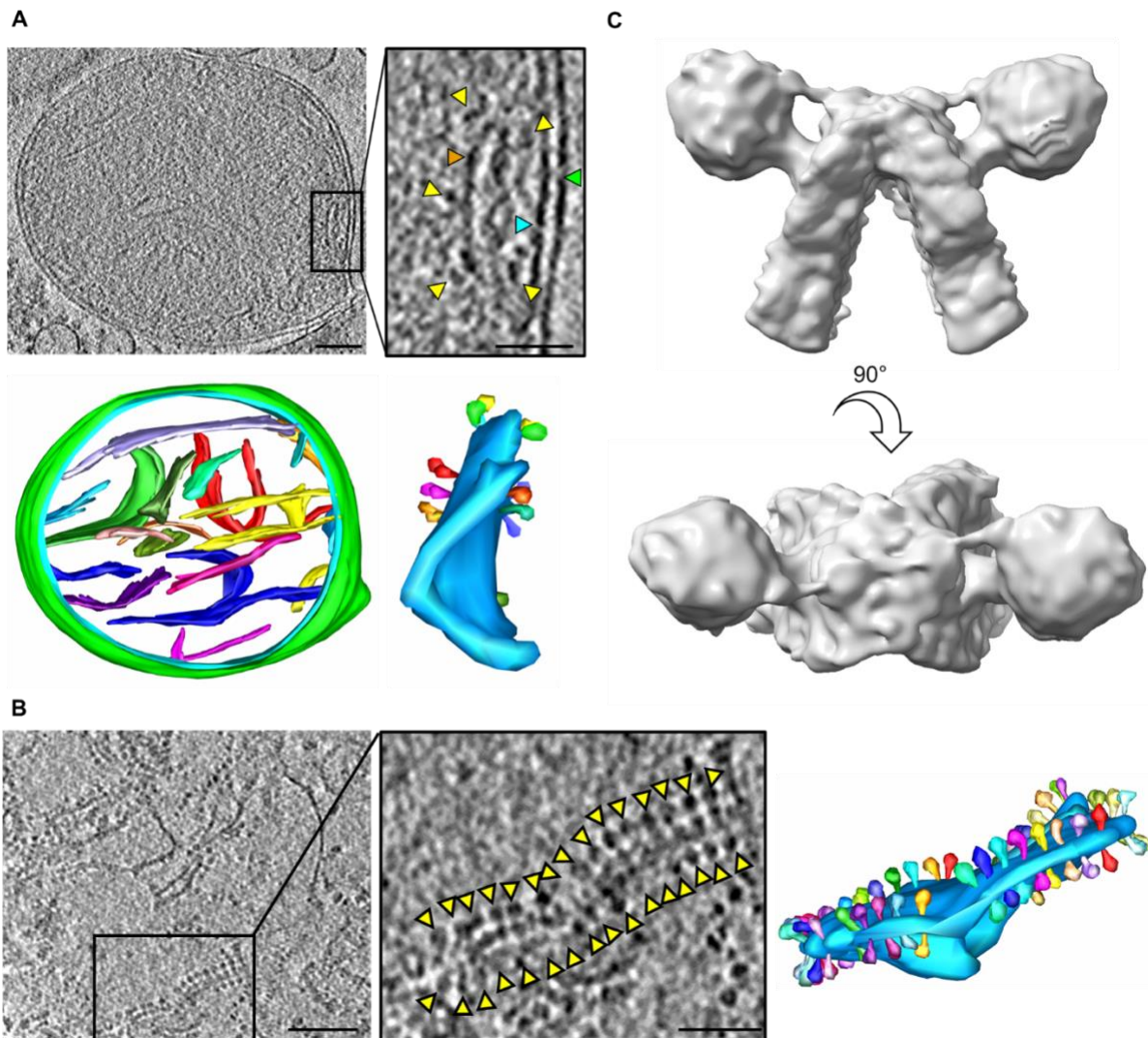
530 **Author Contributions**

531 EB conducted the experiments with *C. elegans* and analysed and quantified all tomographic data. MM
532 assisted with electron microscopy and processing of tomographic data. PB prepared yeast mitochondria
533 for processing by VG. AB conducted bioinformatics analysis. HF purified ATP synthase from *C. elegans* for
534 mass spectrometry analysis. BD and PK provided resources and advice. IC and VG designed the project
535 and obtained the funding. EB and VG wrote the paper. All authors commented on the manuscript.

536

537 **Competing Interest Statement:** The authors declare no competing interests.

538 **Figures**



539

540 **Figure 1. ATP synthase dimer rows, and sub-tomogram average of the ATP synthase dimer from *C.***

541 ***elegans.***

542 **(A)** Tomographic slice through a whole *C. elegans* mitochondrion (top) and corresponding segmentation

543 (bottom; outer membrane green, inner membrane light blue, and a different colour for each crista

544 membrane). The boxed region shows an enlarged image of a single crista membrane, with green, blue and

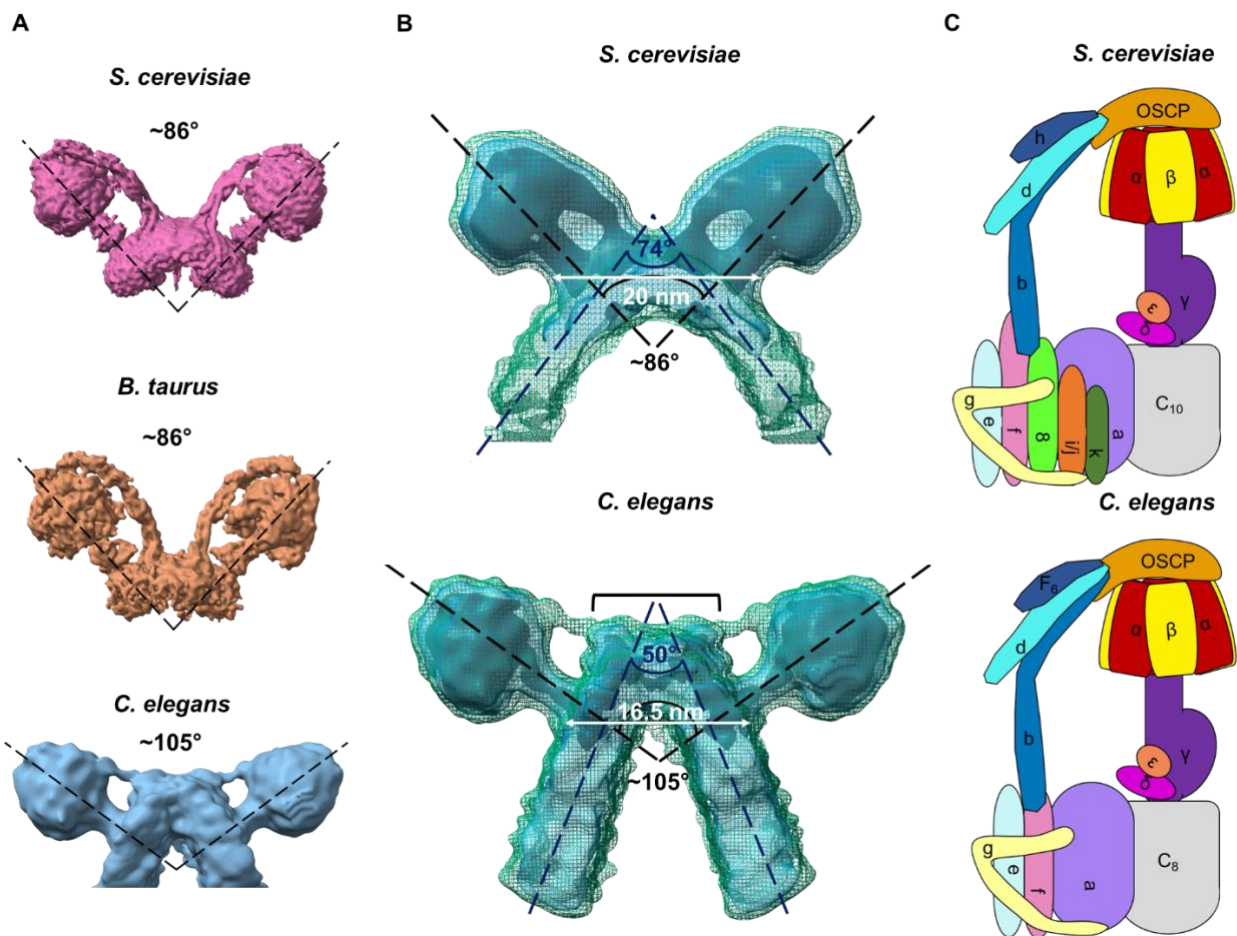
545 orange arrowheads indicating the outer, inner and crista membranes respectively, and yellow arrowheads

546 indicating ATP synthase F₁ heads. The crista membrane is coloured light blue in the corresponding

547 segmentation; each ATP synthase dimer pair is coloured differently. **(B)** Tomographic slice through *C.*

548 *elegans* isolated crista membranes (left, yellow arrowheads indicating ATP synthase F₁ heads) and

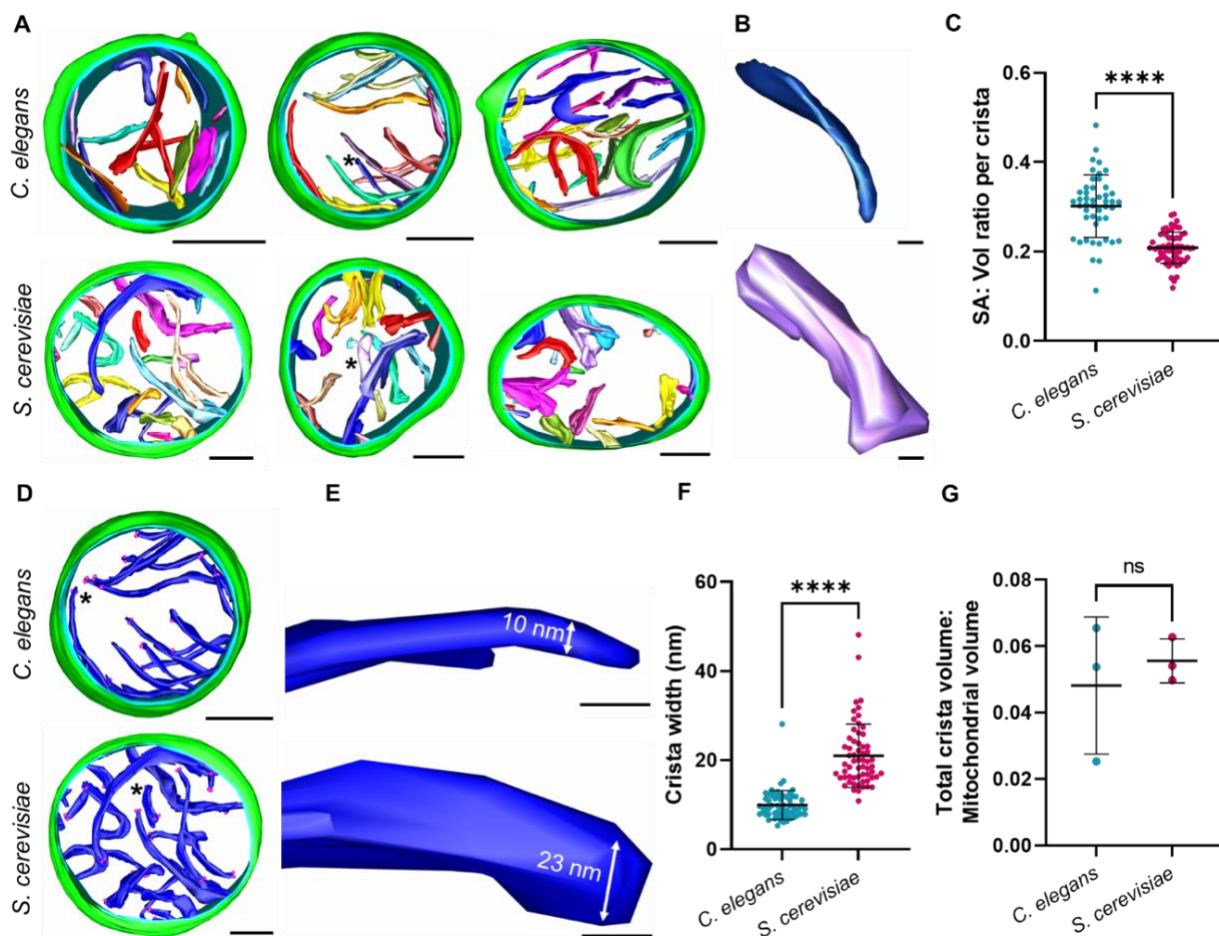
549 corresponding segmentation (right). The boxed region shows an enlarged image of a single crista
550 membrane, with the corresponding segmentation coloured as in panel A. Scale bars, 100 nm for
551 tomograms, and 50 nm for enlarged views of crista membranes. **(C)** Sub-tomogram average of the *C.*
552 *elegans* ATP synthase dimer at a resolution of 38.6 Å [EMD-16216]. Upper panel shows side view, lower
553 panel shows top down view.



554

555 **Figure 2. The *C. elegans* ATP synthase compared to other species.**

556 **(A)** Structures depicting the range of average dimer angles observed in *S. cerevisiae* [EMD-7067] (30),
 557 bovine heart [EMD-11436] (29), and *C. elegans* (this work, [EMD-16216]), using the highest resolution
 558 structures available. **(B)** Direct comparison between *S. cerevisiae* [EMD-2161] (11) and *C. elegans* ATP
 559 synthase sub-tomogram averages, with the angle between F₁ dimer heads, the angle of crista membrane
 560 curvature, and crista membrane width indicated. A bracket highlights the additional density at the *C. elegans*
 561 dimer interface not apparent in *S. cerevisiae*. Black, transparent blue and dark green mesh represent
 562 decreasing threshold levels for the averages. **(C)** Cartoon detailing occurrence of ATP synthase subunits
 563 in *S. cerevisiae* and *C. elegans*, each labelled with corresponding nomenclature for the species (details in
 564 Table S1).



565

566 **Figure 3. Morphology of mitochondria isolated from *C. elegans* and *S. cerevisiae*.**

567 **(A)** Tomographic segmentations of *C. elegans* and *S. cerevisiae* mitochondria are displayed (green, outer

568 mitochondrial membrane; blue, inner mitochondrial membrane; multi-colour, crista membranes). See Movie

569 S1 (*C. elegans*) and Movie S2 (*S. cerevisiae*). **(B)** Enlarged examples of crista membranes (location

570 indicated by asterisks in A) to highlight the flatter cristae morphology in *C. elegans* mitochondria compared

571 to *S. cerevisiae*. **(C)** The mean surface area to volume ratio per crista (n = 3 mitochondria for each organism,

572 with n=47 cristae for *C. elegans* and n=63 cristae for *S. cerevisiae*) was calculated from the segmentations

573 shown in (A). **(D)** A single tomographic segmentation from each organism is shown with all crista coloured

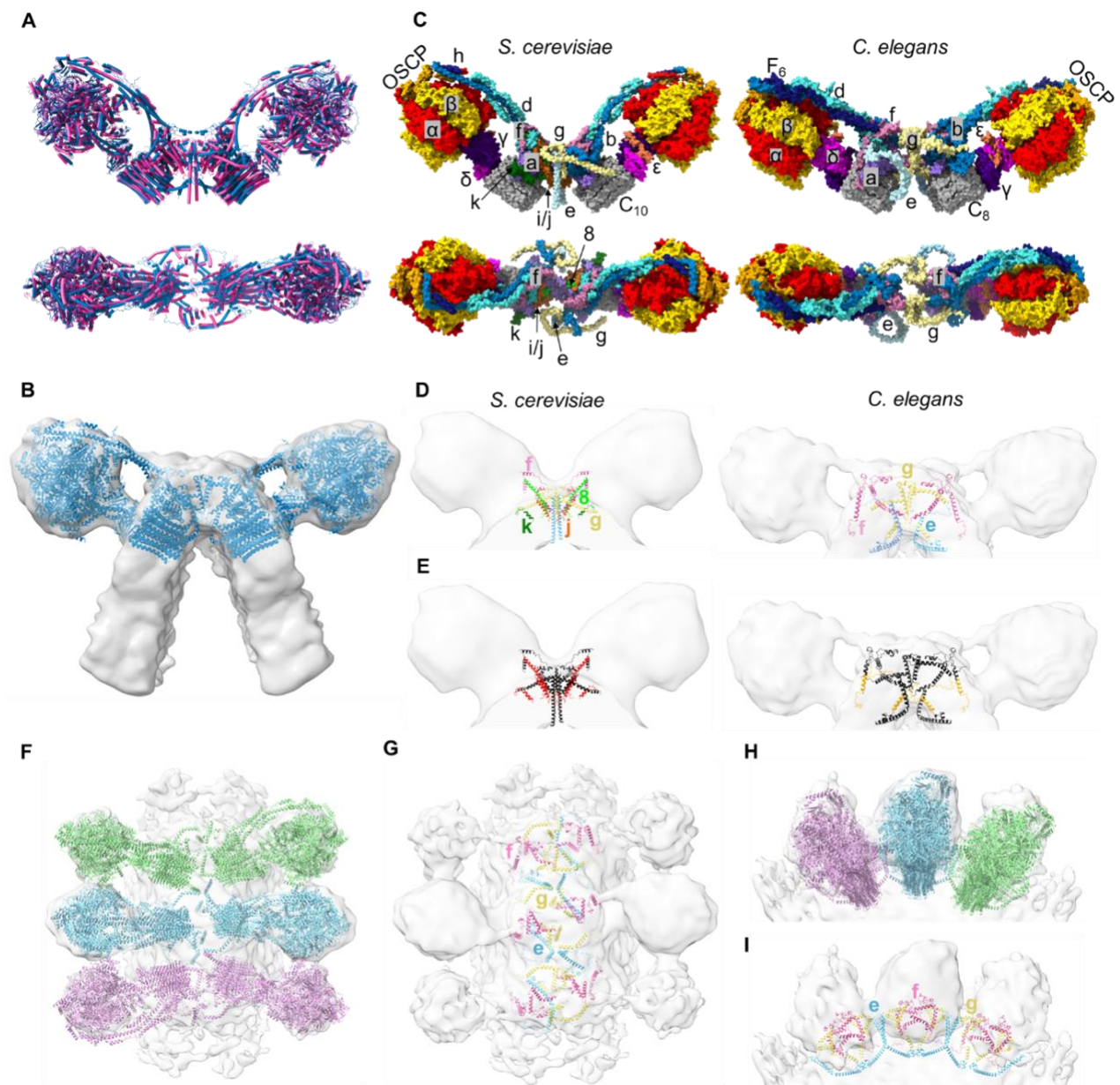
574 blue. Pink dots indicate distances used to measure width at the crista tips. **(E)** Close up of a single crista

575 membrane from each organism (location indicated by asterisks in D, with crista tip width specified). **(F)** The

576 mean crista width (n= 63 crista tips for *C. elegans* and n= 61 for *S. cerevisiae*) was calculated from the

577 segmentations shown in (A). **(G)** The mean total crista volume relative to mitochondrial volume (n = 3

578 mitochondria for each organism) was calculated from the segmentations shown in (A). Error bars in C, F
579 and G show standard deviation of the mean and significance values were calculated using Welch's t-test
580 for panel C or using the Mann-Whitney U-test for panels F and G. **** $p \leq 0.0001$. Scale bars in A & D, 200
581 nm; in B & E, 20nm.
582



583

584 **Figure 4. AlphaFold homology model of the *C. elegans* ATP synthase dimer.**

585 **(A)** AlphaFold predictions for *C. elegans* ATP synthase subunits (blue) overlaid with the atomic model of
 586 the yeast ATP synthase dimer ([PDB 6B8H] (30), pink), using cylinder representation. Predicted models
 587 were fitted onto 6B8H using MatchMaker in ChimeraX. **(B)** Two monomers from the *C. elegans* ATP
 588 synthase homology model (helical representation) fitted to the sub-tomogram average of the *C. elegans*
 589 ATP synthase dimer to generate the correct dimer angle. **(C)** Surface view of *S. cerevisiae* and *C. elegans*
 590 ATP synthase dimer models coloured by chain in side (top) and top-down (bottom) views. Subunits are

591 annotated and shown as α , red; β , gold; γ , indigo; δ , magenta; ϵ , coral; c, grey; a, purple; b, blue; d,
592 turquoise; h/F₆, navy; OSCP, orange; e, pale blue; f, pink; g, yellow; i/j, brown; k, dark green; 8, lime. All
593 subunits are labelled in the side views with the exception of 8 which is buried. Only the dimer interface
594 subunits are labelled in the top-down views. **(D)** Left, dimer interface subunits in the *S. cerevisiae* atomic
595 model [6B8H] (30) coloured by chain and fitted to an *S. cerevisiae* sub-tomogram average [EMD-2161]
596 (11). Right, dimer interface subunits in the *C. elegans* homology model coloured by chain fitted to the *C.*
597 *elegans* sub-tomogram average. Subunits are annotated with the same colours as panel C. **(E)** As per (D),
598 but with all subunits colored black, highlighting subunits missing in *C. elegans* relative to *S. cerevisiae* (j, k
599 and 9) in red (left) and extensions in *C. elegans* subunits e, f and g relative to *S. cerevisiae* in orange (right).
600 **(F)** Top down view of the *C. elegans* ATP synthase dimer homology model fitted to the sub-tomogram
601 average showing sequential dimer pairs in a row. **(G)** As per (F), but exclusively showing dimer interface
602 subunits e, f and g coloured by chain as per panels C and D. **(H)** and **(I)** show the same interactions as in
603 (F) and (G) respectively but viewed from the side of a dimer row.

604 **Supporting Information for**

605 Cryo-electron tomography of *C. elegans* mitochondria reveals how the

606 ATP synthase dimer interface shapes crista membranes

607

608 Emma Buzzard, Mathew McLaren, Piotr Bragoszewski, Andrea Brancaccio, Holly Ford, Bertram

609 Daum, Patricia Kuwabara, Ian Collinson & Vicki A.M. Gold.

610

611

612 **This PDF file includes:**

613 Supporting text

614 Figures S1 to S12

615 Tables S1 to S3

616 Legends for Movies S1 to S2

617 SI References

618

619 **Other supporting materials for this manuscript include the following:**

620 Movies S1 to S2

621

622 **Supporting Information Text**

623 **Extended methods**

624

625 **ATP synthase purification from *C. elegans* mitochondria**

626 *C. elegans* ATP synthase was purified using a His-tagged IF₁ as bait, following a scaled down
627 protocol designed for purification of bovine dimers (73, 74). Residues 1-60 of the *C. elegans* F-
628 ATPase inhibitor protein IF₁ fused to a hexa-histidine tag (cel1-60His), were overexpressed from
629 a pRSFDuet plasmid in *E. coli* BL21 (DE3), and purified by affinity chromatography on a 5 mL
630 Nickel-Sepharose column (Cytiva) attached to an ÄKTA purification system (Cytiva). Fractions
631 enriched in IF₁ were concentrated to ~50 mg/mL with a VivaSpin concentrator (molecular weight
632 cut-off 3 kDa; Sartorius).

633

634 *C. elegans* mitochondria were washed in a phosphate buffer (50 mM sodium hydrogen phosphate,
635 100 mM sucrose and 0.5 mM EDTA) and then centrifuged at 13,700 x g for 45 minutes at 4°C. This
636 wash step was repeated twice to remove endogenous *C. elegans* IF₁. Phosphate-washed
637 mitochondria (~16 mg) were solubilised for 30 minutes at 18°C at 7.65 mg/ml with digitonin (0.92%
638 w/v) and DDM (0.76% w/v). The resulting extract was centrifuged at 24,000 x g for 20 minutes at
639 4°C, and cel1-60His was added to the supernatant at 2.7 µg per 1 mg mitochondria to form
640 ATPase:cel1-60His complexes. A solution of 200 mM ATP, 200 mM MgSO₄, and 400 mM Trizma
641 (pH 8.0) was also added at 15 µl/ml before incubating for 15 minutes at 37°C, with further additions
642 of this solution being added at 5 minute intervals. Precipitate was removed by centrifugation at
643 24,000 x g for 10 minutes at 4°C. NaCl and imidazole were added to the clarified sample to reach
644 final concentrations of 150 mM and 25 mM respectively. This final extract was applied to a 1 mL
645 HisTrap FF Nickel Column (Cytiva) installed on an ÄKTA purification system (Cytiva) and
646 equilibrated in a buffer containing 20 mM Tris, pH7.4, 150 mM NaCl, 2 mM ATP, 2 mM MgSO₄,
647 10% (v/v) glycerol, 0.1% (w/v) glyco-diosgenin (GDN) and a 0.1 mg/mL phospholipid mix. The
648 ATPase:cel1-60His complexes were eluted from the column by addition of a linear gradient of
649 imidazole up to 500 mM over 10 mL. 0.5mL fractions were collected and run on an SDS-PAGE gel
650 to confirm which fractions contained the ATPase:l1-60His.

651

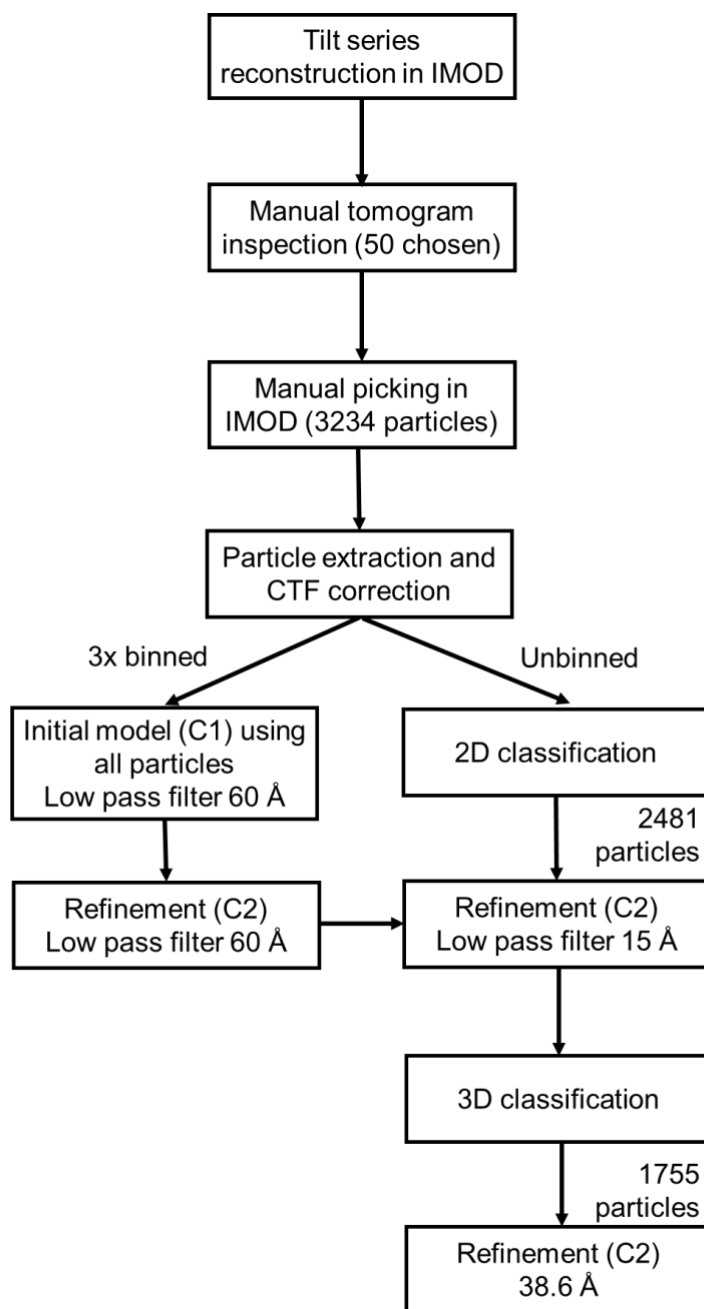
652 **Nano-LC Mass Spectrometry**

653 The sample of ATP synthase was run on a 10% SDS-PAGE gel until the dye front had migrated
654 approximately 1cm into the separating gel. The gel lane was then excised as a single slice and
655 subjected to in-gel tryptic digestion using a DigestPro automated digestion unit (Intavis Ltd.). The
656 resulting peptides were fractionated using an Ultimate 3000 nano-LC system in line with an Orbitrap
657 Fusion Lumos mass spectrometer (Thermo Scientific). Spectra were acquired with Xcalibur 3.0
658 software (Thermo Scientific).

659

660 The raw data files were processed and quantified using Proteome Discoverer software v2.1
661 (Thermo Scientific) and searched against the UniProt *Caenorhabditis elegans* database
662 (downloaded October 2022; 26728 sequences) using the SEQUEST HT algorithm. Search criteria
663 included oxidation of methionine (+15.995Da), acetylation of the protein N-terminus (+42.011Da)
664 and methionine loss plus acetylation of the protein N-terminus (-89.03Da) as variable modifications
665 and carbamidomethylation of cysteine (+57.021Da) as a fixed modification. Searches were
666 performed with full tryptic digestion and a maximum of 2 missed cleavages were allowed. The
667 reverse database search option was enabled and all data was filtered to satisfy false discovery rate
668 (FDR) of 5%.

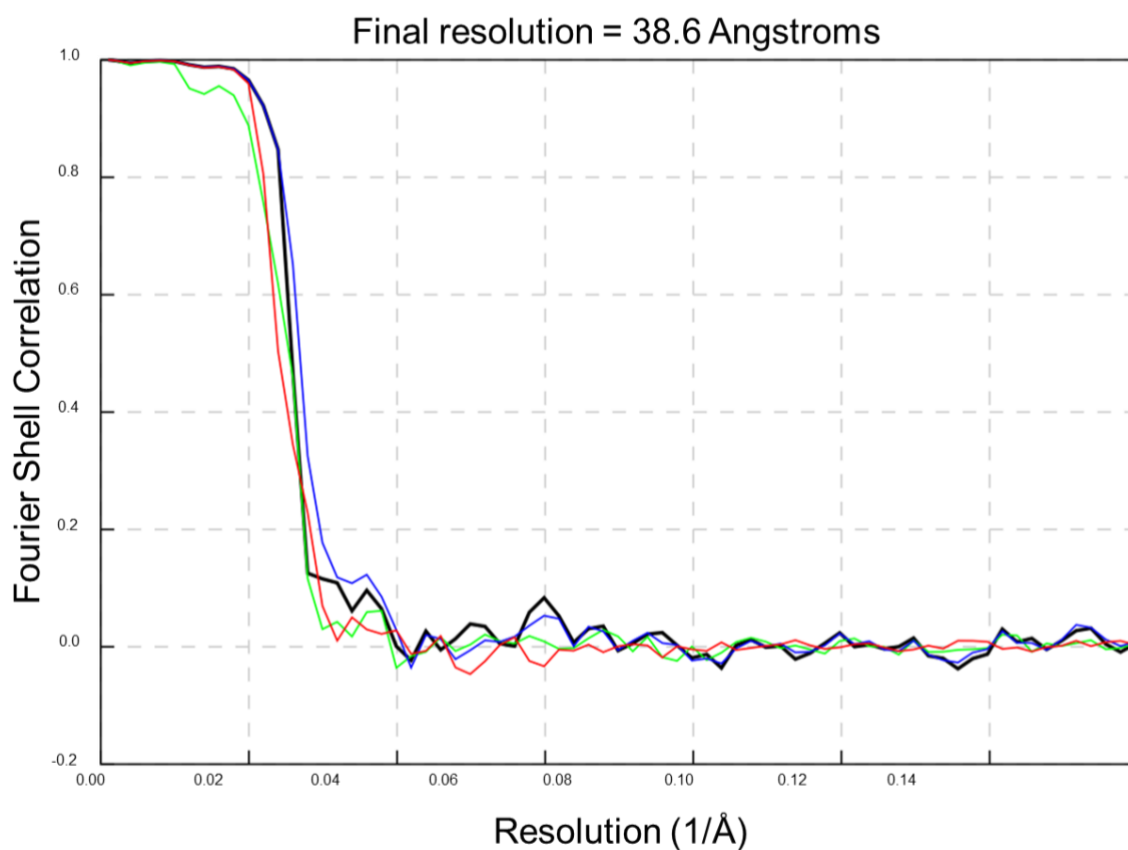
669



670

671 **Figure S1. Flow chart of tomogram processing and sub-tomogram averaging using IMOD**

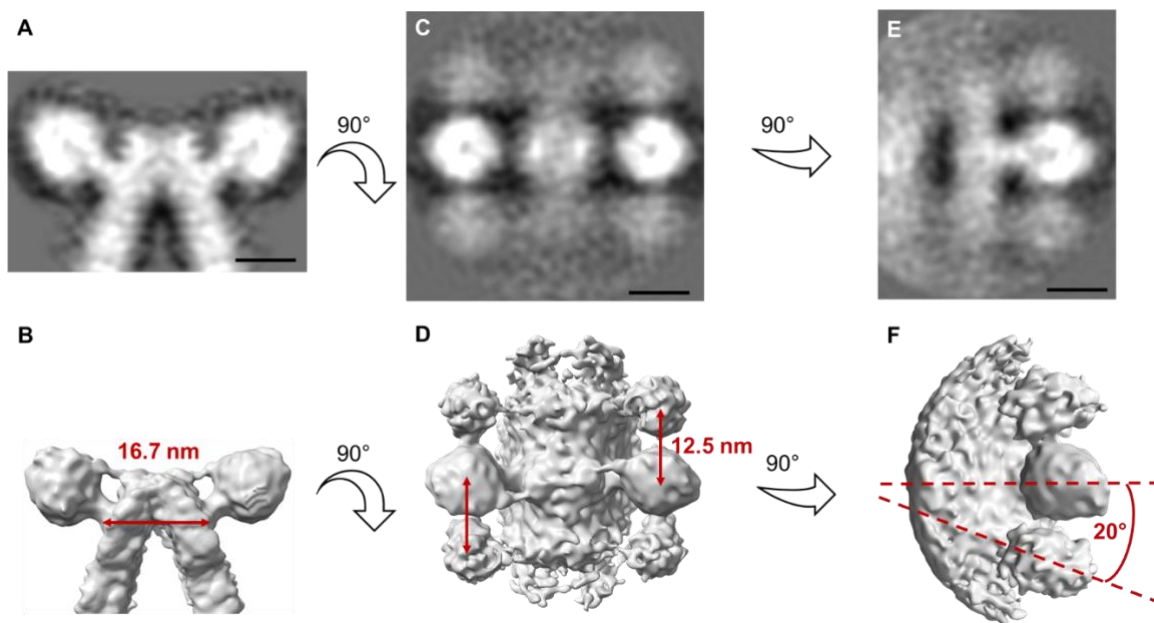
672 **and Relion.**



673

674 **Figure S2. Fourier Shell Correlation (FSC) for the *C. elegans* ATP Synthase sub-tomogram**
675 **averaging map.** The FSC curve is an output from Relion 3.1. The corrected FSC is shown in black,
676 unmasked FSC in green, masked FSC in blue, and phase randomised masked FSC in red.

677



678

679 **Figure S3. Inter-dimer distance and angle between consecutive dimer heads in oligomeric**

680 **rows of *C. elegans* ATP synthase dimers. (A)** 2D projection showing side view of a masked map

681 of the *C. elegans* ATP Synthase dimer. **(B)** Side view shown in 3D, with distance between central

682 stalks indicated. **(C)** 2D projection showing top down view of an unmasked map of the *C. elegans*

683 ATP synthase dimer. **(D)** Top down view in 3D with inter-dimer distance indicated. **(E)** 2D projection

684 showing side view (rotated 90° compared to A) of an unmasked map of the *C. elegans* ATP

685 Synthase dimer. **(F)** Side view in 3D, with inter-dimer angle indicated. All indicated measurements

686 were made in IMOD. Scale bars, 10 nm.

687

697

698 **Subunit b (isoform 2)**

```

sp|Q19126|AT5F2_CAEEL      MSLSRCLPLGQNRVIIIPARLAHAASTQAAAATDDAPNFFQKLAHRFGVPLKGEAHAP 60
sp|P05626|ATPF_YEAST      MSM-----SM-----GVRGLALR---SVS 16
sp|P13619|AT5F1_BOVIN     MLS-----RV-----VLS--AAA--AAA 14
*                               :                               .

sp|Q19126|AT5F2_CAEEL      KSMFEDCNKEWSAPELPAIPKDFKEHPDRDLVNYYPARPMYPPKSRLLMMPDSWFTPF 120
sp|P05626|ATPF_YEAST      KTLFSQG---VRCPSMVIGA---RYM-SSTPEKQT---DPKAKANSIINAIPGN---NI 62
sp|P13619|AT5F1_BOVIN     PSLKNAA---LLGPGVLQAT---RIFHTGQPSLAPVPLPEHGGKVRFGLIPEEFFQFL 67
: : . * : : : * : : : * : : :
: : . * : : : * : : :

sp|Q19126|AT5F2_CAEEL      QKVTGVSGPYLFFGGLFAFLVNKELWVFEEQGHMTVGWILFYLLVTRTAGYKIDQGLYNG 180
sp|P05626|ATPF_YEAST      LTKTGVLG---TSAAAVIYAISNELYVINDESILLTFLGFTGLVAKYLAPAYK-----D 114
sp|P13619|AT5F1_BOVIN     YPKTGVTGPYVLGTGLLILYLLSKEIYVITPETFSAISTIGFLVYIVKKGASVG-----E 122
*** * . . . : : * : : : : * : : :

sp|Q19126|AT5F2_CAEEL      YQERVNF-----FKGLIQEDLKEAVEFKTSAKQTESLNSIKESYPTALKESSMALQL 232
sp|P05626|ATPF_YEAST      FADARMKKVSDVLNASRNKHVEAVKDRID-----SVSQLQNAETTKVLFFDVSKETVELES 170
sp|P13619|AT5F1_BOVIN     FADKLNEQKIAQLEEVKQASIKQIQDAID---MEKSQQALVQKRHYLFDVQRNNIAMAL 178
: : : : : : : : : : : : : : : : : : : : : : :

sp|Q19126|AT5F2_CAEEL      EATYRKNVQSVATELKRRIDYLKETEESKARVEREQLLKLINSEVDKEFSDRSFKDKYLQ 292
sp|P05626|ATPF_YEAST      EAFELKQKVELAEAKAVLDSWVRYEASLRQLEQRQLAKSVISRVQSELGNPKFQEKVLQ 230
sp|P13619|AT5F1_BOVIN     EVTYRERLHRVYREVKNRLDYHISVQNMMRQKEEHMINNWVEKRVVQSISAQQE-KETIA 237
* . : . : * * : * : : * : : : : : : * . . . . : : :

sp|Q19126|AT5F2_CAEEL      NAIQQLKGLNVQL----- 305
sp|P05626|ATPF_YEAST      QSISEIEQLLSKLK----- 244
sp|P13619|AT5F1_BOVIN     KCIADLKLLSKKAQAQPVM 256
: . * : : : * :

```

699

700

701 **Subunit d**

```

tr|Q17763|Q17763_CAEEL    MSGAAKRVATSSVNWSKLAER--LVPEHAAELTRVKGVSGTFQSAVSQLPADLPKIDFAA 58
sp|P30902|ATP7_YEAST      --MSLAKSAANKLDWAKVISSLRITGSTATQLSSFKKRNDEARRQLLELQSQPTEVDFSH 58
sp|P13620|ATP5H_BOVIN     --MAGRKLLAKTIDWVAFGEI--IPRNQKAVANSLKSWNETLTSRLATLPEKPPAIDWAY 56
: : * . : : * . . : . : . * . : * . : : :

tr|Q17763|Q17763_CAEEL    LKKALPAHASA--VLDSLQKQYESVKIPYGEVPAEYL-----KEVDQWVDYNNARIK 107
sp|P30902|ATP7_YEAST      YRSVLKNTSVIDKIESYVKQYKPVKIDASKQLQ-----VIESFEKHAMTNAK 105
sp|P13620|ATP5H_BOVIN     YKANV-AKAG--LVDDFEKFNALKVPIPEDKYTAQVDAEEKEDVKSCAEFLTQSKTRI- 112
: : : : : * : : : * : : : : : : :

tr|Q17763|Q17763_CAEEL    LHEVKVADGLQEAKKVEEKWAKAPPVEHFDRQHFVEYFPAHFYDLRYQNRIPDPCNIGLN 167
sp|P30902|ATP7_YEAST      ETESLVSKELKDLQSTLDNIQSARPFDELTVDDLTKIKPEIDAKVEE-----MVKKGKW 159
sp|P13620|ATP5H_BOVIN     -----QEYEKELEKMRNIIPFDMTIEDLNEVFPETKLDKKYYPWHPRIETL- 161
: : : : : * . : : : : * . . .

tr|Q17763|Q17763_CAEEL    ETPEIENRFKDYKVLRRADKVDDH 191
sp|P30902|ATP7_YEAST      DVPGYKDRFGNLNVM----- 174
sp|P13620|ATP5H_BOVIN     ----- 161

```

702

703 **Subunit F₆**

```

tr|O16517|O16517_CAEL  -----MFRAVQSV-----RS---L-----ST---TAACRQDLIQQTFFVTKIREIAK--- 35
sp|Q12349|ATP14_YEAST  -----MFPIASRRILLNASVLPRLCNRFNFTTRISY---NVIQDLYLRELKDTKLAPS 51
sp|P02721|ATP5J_BOVIN  MILQRLFRLLSSAV----QSAISV-SWRRNIGITAVAFNKELDPVQKLFVDKIREYRTK-- 53
                        :* . * : : : * : : : :
tr|O16517|O16517_CAEL  ---NAGNLANSDPVKKALQEELNRLATKFLANADVSKLPTNFEAAKVDSAVQSALE 91
sp|Q12349|ATP14_YEAST  TLQDAEGNVKPNPPQKPNLPELELQ-----GPEALKAYTE--QNVETAHVA---KESEE 101
sp|P02721|ATP5J_BOVIN  --RQTSGGPVDAGPEYQQLDRELFKLLQMYGKADMNTFPN--FTFDPKFEVVE----- 104
                        * . * : * . : .. : ..* :.
tr|O16517|O16517_CAEL  GQTLASLLEGVKKD-HSEYVASRDAKKAQEAARNAALKQ 129
sp|Q12349|ATP14_YEAST  -----GESEPIEEDWLVLDDAETKESH----- 124
sp|P02721|ATP5J_BOVIN  -----KP-QS----- 108
                        : ..

```

704

705

706 **Subunit OSCP**

```

tr|P91283|P91283_CAEL  MAQ-----LMKRGFSTS--AALAKAQLVKTPIQVHGVEGRYAAALYSAGHKQNKLDQI 51
sp|P05626|ATPF_YEAST  -----MSMSMGVRLGALRSVSKTLFSQGVRCPSMVIGA--RYMSST---PEKQT----- 44
sp|P13621|ATPO_BOVIN  MAALAVSGLSQVRCFSTS--VVRPFACLVRPPVQIYGIIEGRYATALYSAASKQNKLEQV 58
                        * : : : * : * * : : *
tr|P91283|P91283_CAEL  STDLNNVRSVYKDNKKFQEFVLDPTLKANKK-----KTAIEAI----- 89
sp|P05626|ATPF_YEAST  -----DPKAKANSIINAIPGNILTKTGVLTSAAAVIYAI SNELYVINDESI 92
sp|P13621|ATPO_BOVIN  EKELLRVGQILKEPKM-AASLLNPPYKRSVK-----VKSLSDM----- 95
                        : * : : : : : : : :
tr|P91283|P91283_CAEL  --STKLGLTKETGNFLGLLA--ENGRLNKLESVV-----SSFESI--MRAH 129
sp|P05626|ATPF_YEAST  LLLTLFLGFTGLVAKYLAPAYKDFADARMKKVSDVNLASRNKHVEAVKDRIDSVSQLQNV 152
sp|P13621|ATPO_BOVIN  --TAKEKFSPLTSNLINLLA--ENGRLTNTPAVI-----SAFSTM--MSVH 135
                        : : : : : : : : : * : : : :
tr|P91283|P91283_CAEL  -RGELFVQVTS-AEELSSS----NQK---ALSDALSKIGKSGQKLT-V-TYAVKPSIL 176
sp|P05626|ATPF_YEAST  ETTKVLFDVSKETVLESEAFELKQFVELAHEAKAVLDSWVRYEASLRQLEQRQLAKSVI 212
sp|P13621|ATPO_BOVIN  -RGEVPCTVTT-ASALDEA----TLT----ELKTVLKSFLSKGQVVK-L-EVKIDPSIM 182
                        : : * : : * : : : : * : : : * : :
tr|P91283|P91283_CAEL  GGLVVTIGD----KYVDLSIASRVKQKDALATAI 207
sp|P05626|ATPF_YEAST  SRVQSELGNPKFQEKVLQSQSIS-EIEQLLSKLK--- 244
sp|P13621|ATPO_BOVIN  GGMIVRIGE----KYVDMSAKTIQKLSRAMREIL 213
                        . : : * : * : : : :

```

707

708 **Figure S4. Multiple sequence alignment for dimer interface and peripheral stalk subunits.**

709 Comparisons were made between *C. elegans* (O16517), *S. cerevisiae* (Baker's yeast strain ATCC

710 204508 / S288c; Q12349) and *B. taurus* (P02721) using Clustal Omega at EMBL-EBI (47–49). In

711 the alignment output, an asterisk (*) indicates a perfect alignment, a colon (:) indicates a site

712 belonging to a group exhibiting strong similarity, and full stop (.) indicates a site belonging to a

713 group exhibiting weak similarity. Residues are coloured according to their biophysical properties.

714 Small and hydrophobic residues are coloured red, acidic residues are coloured blue, basic residues
715 are coloured magenta, and hydroxyl, sulfhydryl, amine and glycine residues are coloured green.
716 Extensions in *C. elegans* subunits relative to both the *S. cerevisiae* and *B. taurus* homologues are
717 underlined in black, deletions are underlined in maroon. Where subunits have multiple isomers, the
718 isomer used in the homology model is used for alignment.

719 **Subunit e (Q21732)**

720 MSAPLKHPNAVVLQPPTVTISPLIRFGRYAALS LGVVYGGFFRLRQIREYHADIREWDHEKAVAAAE

721 EAAK KKKWLAKDEMRYLMQVVNIPFEEGVKQFGVADLYKED

722

723 **Subunit f (Q22021)**

724 MAWFRPPPHTQLRPWVPDAIFIPISRAVERVGVFFYNRVLNKTEVGLFDKRWNKNVHGPYCH

725 WRYYGKLDTKFMDVKLGDLPAWMARREKTPSAFYNEFMRNIWRVHNLYYSGPVYNNTVKVIFR

726 FIFAYSFLNWLVKSHRYVDFQKTMYHW

727

728 **Subunit g (isoform 2) (Q18803)**

729 MAAPKLGFFEKIANLTGALYRHQHAQFPRRFAILKAVGKHELAPPRQADWPAIKADWAKVQSFIQ

730 TGGYKNLSIREGLVYTAVTLEVVFWFFVGEMIGRRYIFGYLVPADYVSKSTKKTVKEQEALAALE

731 N

732

733 **Subunit b (isoform 2) (Q19126)**

734 MSLSRCLPLGQNARVIIPARLAHAASTQAAAATDDAPNFFQKLAHRFQGVPLKGEAHAPKSMFE

735 DCNKEWSAPEPLPAIPKDFKEHPDRDLVNYPYPARPMYPPKSRLLMMPDSWFTPFQKVTGVSG

736 PYLFFGGLFAFLVNKELWVFEEQGHMTVGWILFYLLVTRTAGYKIDQGLYNGYQERVNFFKGLIQ

737 EDLKEAVEFKKTSAKQTESLNSIKESYPTALKESMALQLEATYRKNVQSVATELKRRIDYLKETEE

738 SKARVEREQLLKLINSEVDKEFSDRSFKDKYLQNAIQQLKGLNVQL

739

740 **Subunit d (Q17763)**

741 MSGAAKRVATSSVNWSKLAERLVPEHAAELTRVKGVSGTFQSAVSQLPADLPKIDFAALKKALP

742 AHSAVLDSLQKQYESVKIPYGEVPAEYLKEVDQWVDYNNARIKLHEVKVADGLQEAKKVEEKWA

743 KAPPVEHFDRQHFVEYFPAHFYDLRYQNRIPDPCNIGLNETPEIENRFKDYKVLRRADKVDDH

744

745 **Subunit F₆ (O16517)**

746 MFRAVQSVRSLSTTAACRQDLIQQTFVTKIREIAKNAGNLANSDPAVKKALQEELNRLATKFQLA

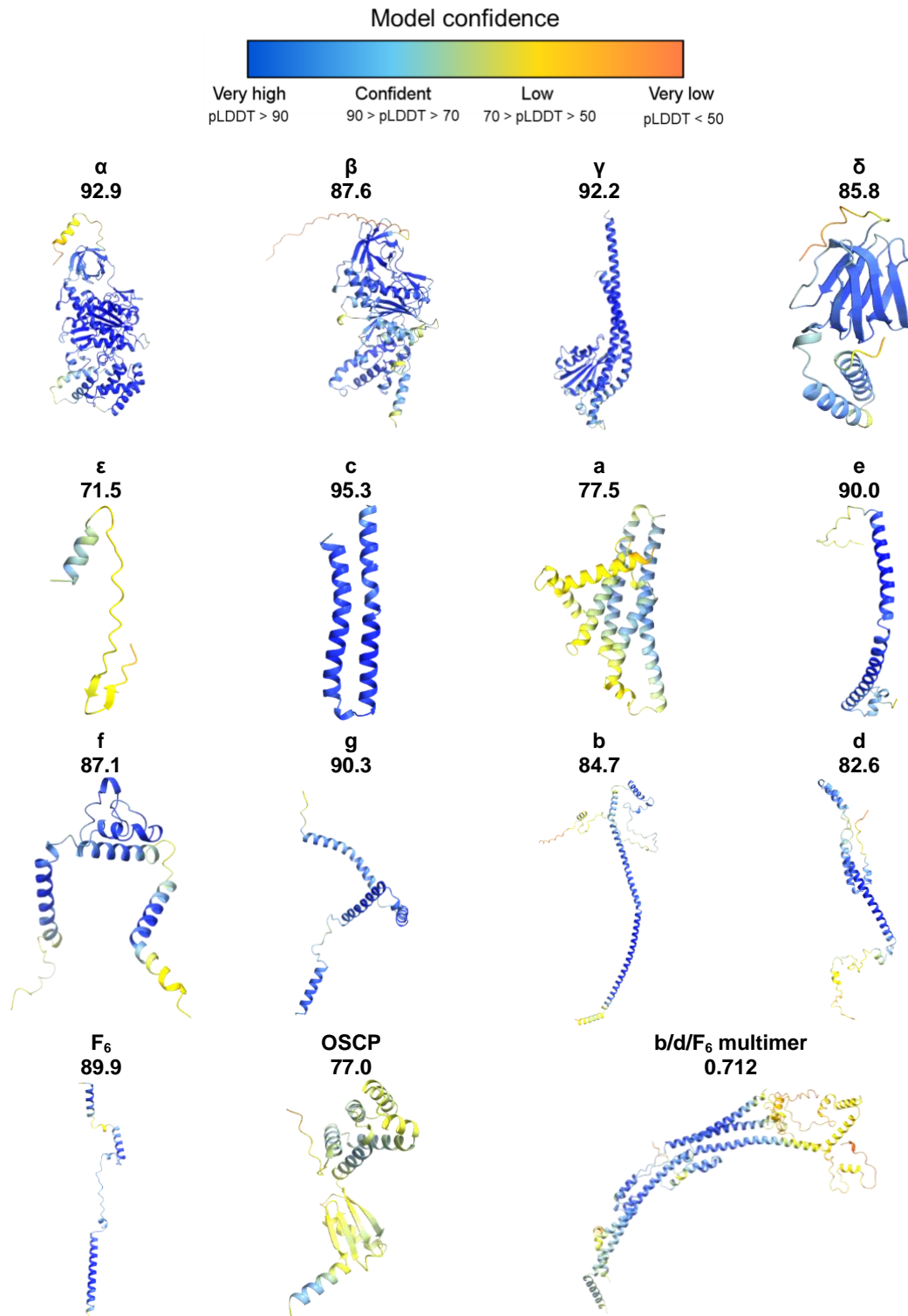
747 NADVSKLPTNFEEAAKVDSAVQSALEGQTLASLLEGVKKDHSEYVASRDAKKAEEQAARNAALKQ

748

749 **Figure S5. Mass spectrometry data for *C. elegans* ATP synthase subunits with significant**
750 **extensions.** The sequence for each subunit of interest is shown and identified with a Uniprot code.
751 The predicted mitochondrial targeting sequences are coloured red. The *C. elegans* specific
752 extensions (revealed in sequence alignments from Fig. S4) are highlighted in yellow. Peptides
753 identified by mass spectrometry are underlined. Where subunits have multiple isomers, the isomer
754 used in the homology model is shown.

755

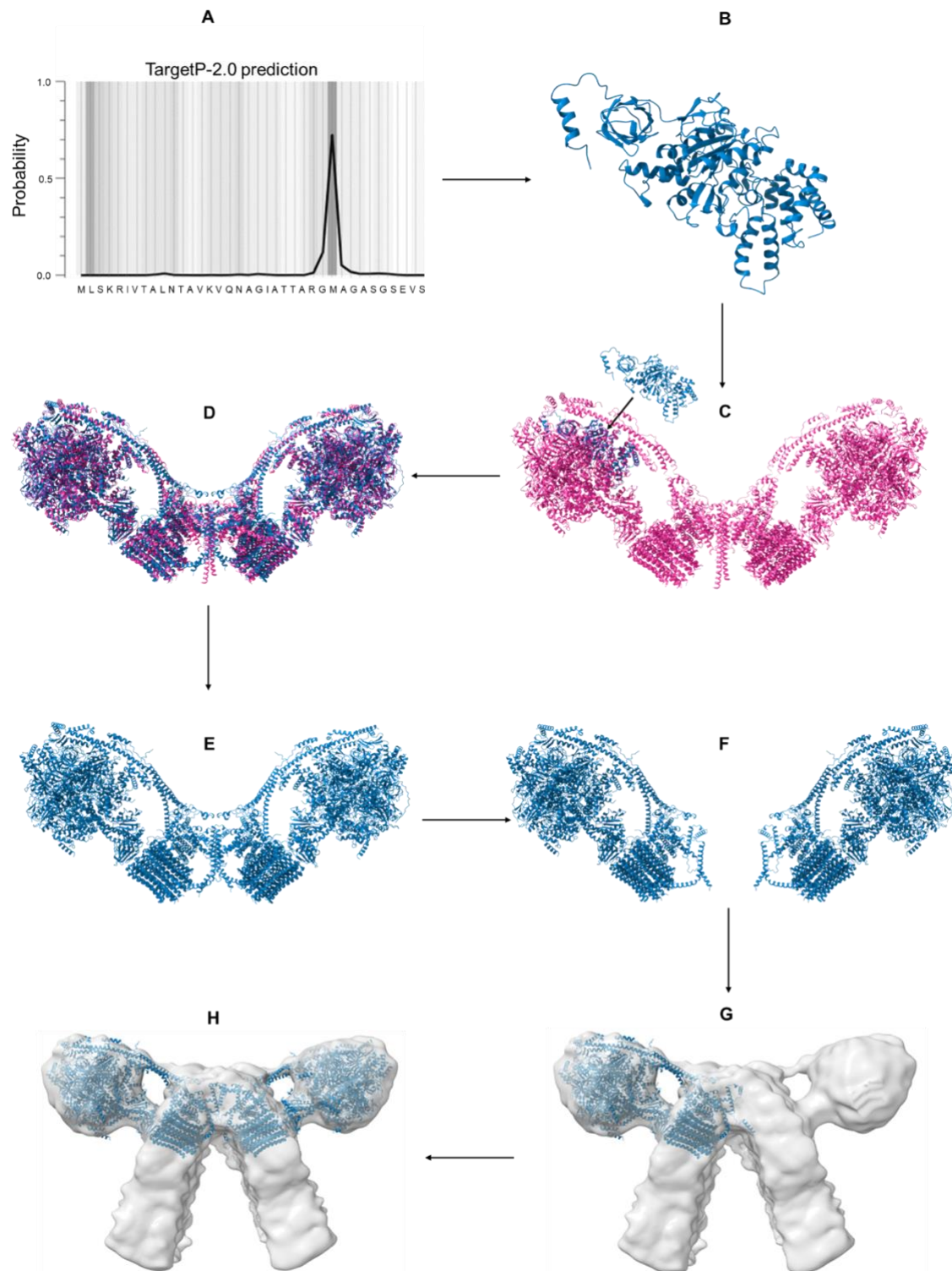
Alphafold predictions gallery



757 **Figure S6. AlphaFold predictions gallery**

758 AlphaFold predictions (41) for each *C. elegans* ATP synthase subunit, coloured by pLDDT score
759 per residue. The pLDDT score is a per-residue measure of local confidence on a scale from 0 –
760 100. The structure of subunits b d and F₆ were predicted as a multimer. The confidence measure
761 for predictions made using AlphaFold multimer (50) is similar, but modified to score interactions
762 between residues of different chains. It is calculated using a weighted combination of predicted-TM
763 score (pTM) and interface predicted-TM score (ipTM), and has a scale from 0-1. The appropriate
764 mean confidence score for each AlphaFold / multimer prediction is shown beneath each subunit
765 name.

766

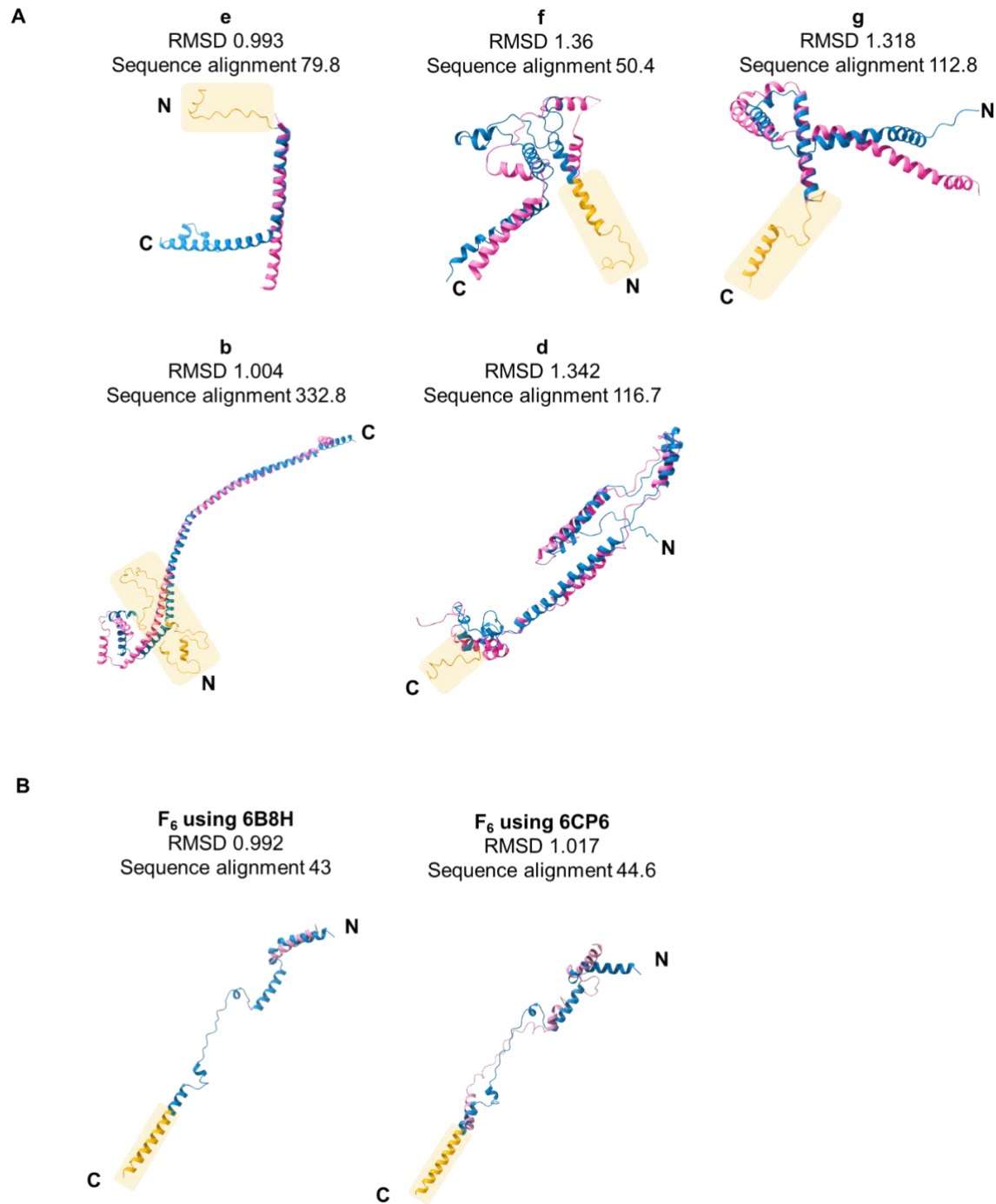


767

768 **Figure S7. *C. elegans* ATP synthase homology model workflow**

769 **(A)** MitoFates (67) or TargetP-2.0 (68) were used to predict the mitochondrial targeting sequence

770 of individual proteins of the ATP synthase, so that the mature protein sequence could be identified.
771 The example shown is the TargetP-2.0 prediction for subunit α . **(B)** AlphaFold was used to predict
772 structures of all mature *C. elegans* ATP synthase subunits; again the example shown is the
773 prediction for subunit α . **(C)** Predicted models were sequentially fitted into the *S. cerevisiae* ATP
774 synthase model [PDB 6B8H] (30) using MatchMaker in ChimeraX. **(D)** The resulting homology
775 model (blue) after all subunits have been fitted to the scaffold provided by 6B8H (pink). **(E)** The
776 homology model without the *S. cerevisiae* scaffolding. **(F)** The *C. elegans* ATP synthase dimer was
777 split into separate monomers. **(G)** The monomers were fitted sequentially into the sub-tomogram
778 average of the *C. elegans* ATP synthase using matchmaker in ChimeraX in order to obtain the
779 correct dimer angle. **(H)** The final homology model of the *C. elegans* ATP synthase dimer fitted into
780 the sub-tomogram average.

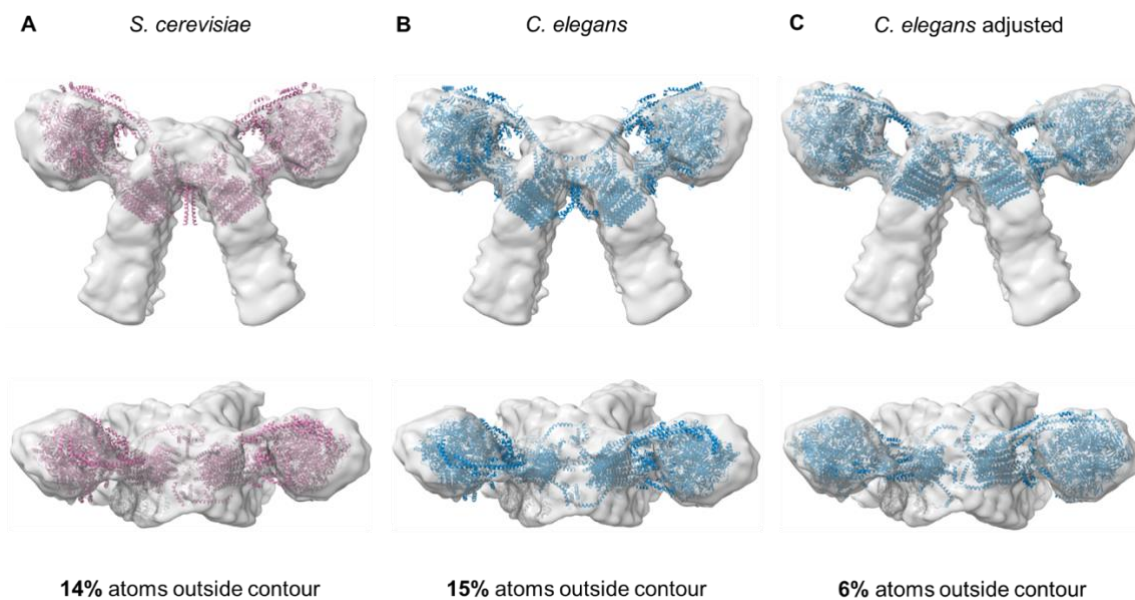


781

782 **Figure S8. Overlays of individual subunits at the dimer interface and peripheral stalk, where**
783 **there are extensions in *C. elegans* homologues compared with *S. cerevisiae*.** *C. elegans*
784 AlphaFold predictions (blue) are overlaid with their *S. cerevisiae* counterparts (6B8H, pink) (30). *C.*
785 *elegans* subunit extensions are highlighted in orange. RMSD values (for pruned atom pairs) and

786 sequence alignment scores output by ChimeraX when using the “fit to model” tool are shown for
787 each overlay. **(A)** Overlays for subunits e, f, g, b and d are taken from the assembled ATP synthase
788 dimers in Fig. 4A. **(B)** Two alternative overlays are shown for subunit F₆. Left, an overlay taken from
789 Fig. 4A as above. However, the *S. cerevisiae* 6B8H (30) structure does not contain the complete
790 density for subunit F₆. Right, an *S. cerevisiae* monomeric atomic model [PDB 6CP6] (72) was used
791 to display a more complete *S. cerevisiae* chain for the overlay.

792

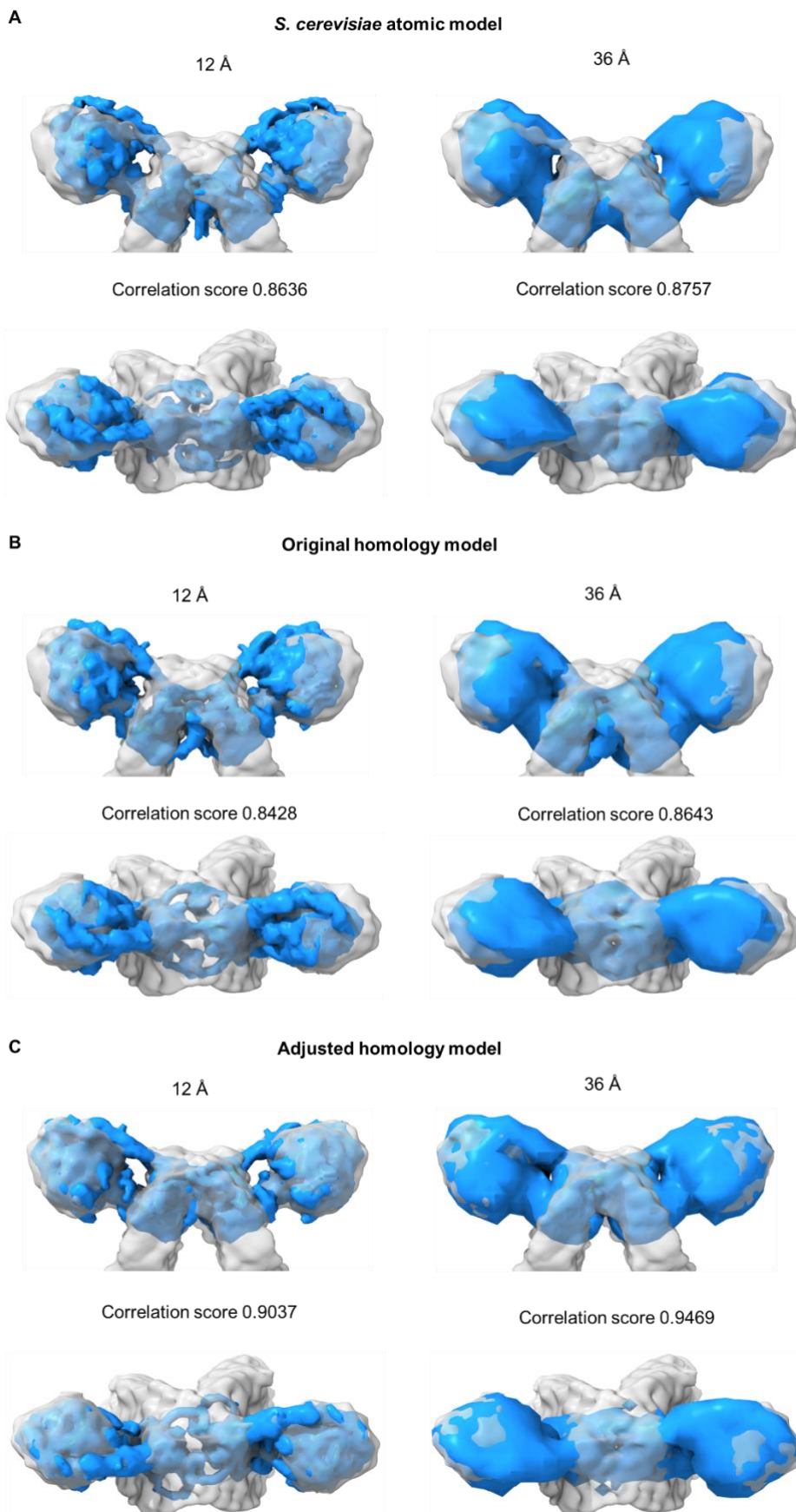


793

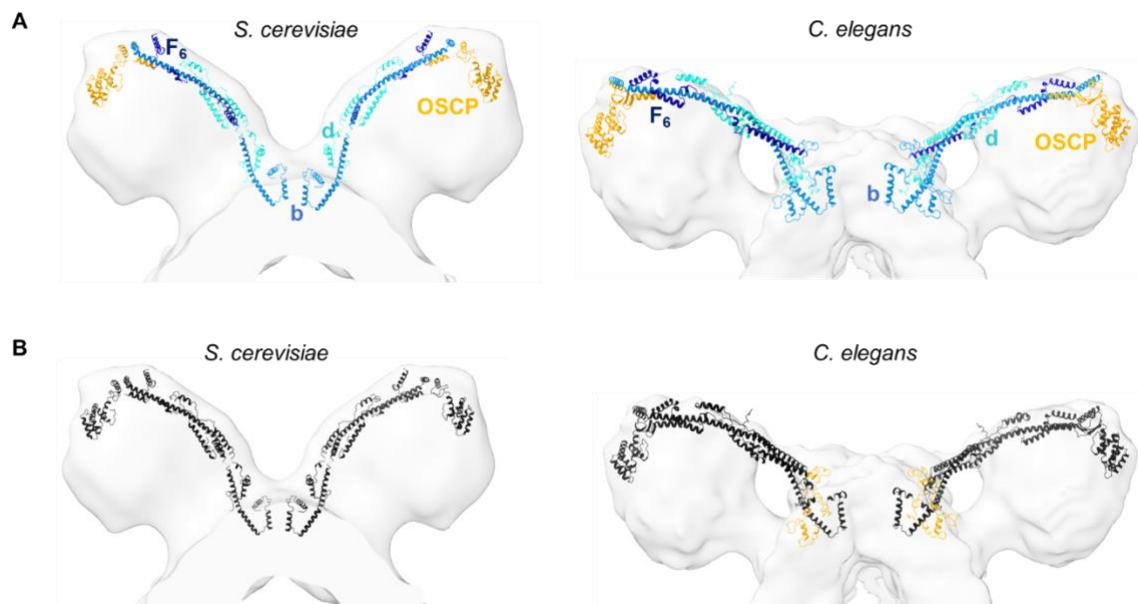
794 **Figure S9. Comparison of different models fitted to the *C. elegans* ATP synthase dimer map.**

795 Different ATP synthase dimer models were fitted into the *C. elegans* ATP synthase *in situ* map. All
796 models were fitted into the map at threshold 0.0429 in ChimeraX, and the percentage of atoms
797 outside the contour is shown for each model. **(A)** The purified *S. cerevisiae* ATP synthase dimer
798 atomic model [PDB 6B8H] (30) shows a poor fit, with 14% of atoms outside the contour. **(B)** The
799 *C. elegans* ATP synthase dimer homology model following scaffolding to the *S. cerevisiae* model
800 also shows a poor fit, with 15% of atoms outside the contour. **(C)** Sequential fitting of monomers
801 from the *C. elegans* homology model shows an improved fit, with only 6% of atoms outside the
802 contour.

803



805 **Figure S10. The *C. elegans* homology model fitted to the *C. elegans* ATP synthase dimer**
806 **sub-tomogram averaging map.** Using the pdb2mrc command in EMAN2 (71), the PDB of the *C.*
807 *elegans* homology model was converted into an MRC map at both 12 Å and 36 Å resolution.
808 Converted pdb2mrc maps (blue) were then fitted to the sub-tomogram averaging map of the *C.*
809 *elegans* dimer (grey) at equivalent threshold levels. Correlation scores between the homology
810 model and sub-tomogram averaging maps are displayed. **(A)** Maps of the 6B8H *S. cerevisiae* ATP
811 synthase atomic model (30) fitted to the sub-tomogram average for reference. **(B)** Maps of the *C.*
812 *elegans* original homology model (without adjusting for dimer angle) fitted to the sub-tomogram
813 average. **(C)** Maps of the dimer angle adjusted *C. elegans* homology model fitted to the sub-
814 tomogram average.



815

816 **Figure S11. Comparison of peripheral stalk subunit arrangement in *S. cerevisiae* vs *C.***

817 ***elegans* ATP synthase dimers. (A) *S. cerevisiae* and *C. elegans* peripheral stalk subunits**

818 **coloured by chain. Subunits are annotated and shown as b, blue; d, turquoise; F₆, dark navy; and**

819 **OSCP, orange. Left, peripheral stalk subunits b, d and OSCP in the 6B8H *S. cerevisiae* atomic**

820 **model (30), and F₆ from the 6CP6 monomeric atomic model (72), fitted to the *S. cerevisiae* sub-**

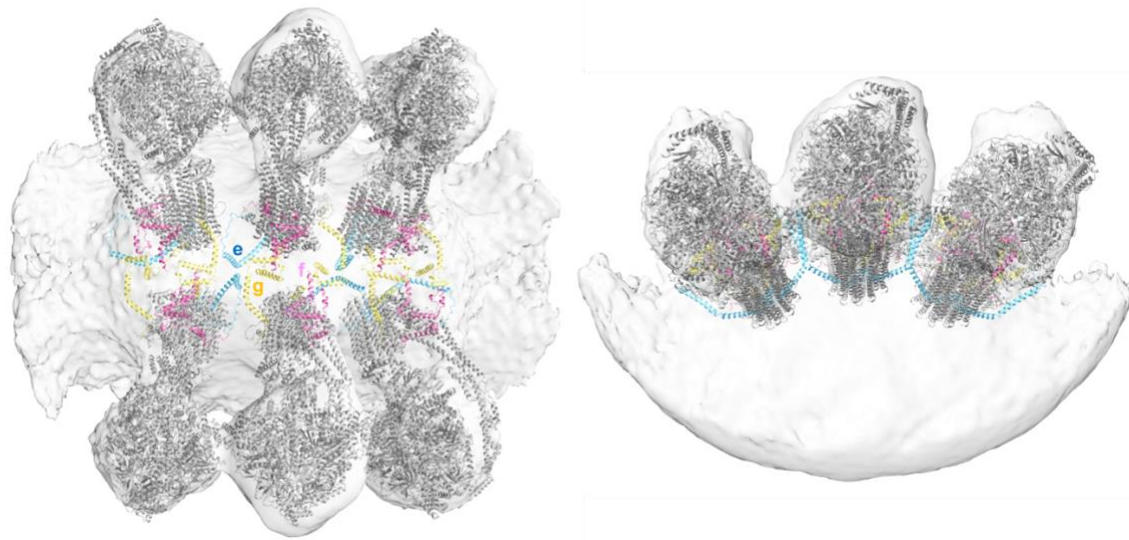
821 **tomogram average [EMD-2161] (11). The chain for F₆ was taken from EMD-6CP6 (see Fig. S8B)**

822 **(72). Right, *C. elegans* homology model fitted to the *C. elegans* sub-tomogram average. (B) As per**

823 **(A), but with all subunits colored black, highlighting extensions in *C. elegans* subunits b, d and F₆**

824 **relative to *S. cerevisiae* in orange.**

825



826

827 **Figure S12. Inter-dimer interactions mediated by subunits e and g in *C. elegans* ATP**
828 **synthase dimer rows.** Top down view (left) and side view (right) of the *C. elegans* ATP synthase
829 homology model (grey) fitted to each dimer pair in the unmasked sub-tomogram average of the *C.*
830 *elegans* dimer. Dimer interface subunits are colored (e, pale blue; f, pink; g, yellow) to highlight
831 extensive inter-dimer interactions mediated by subunits e and g.

832

833 **Table S1. Nomenclature for homologues of ATP Synthase subunits**

<i>C. elegans</i>	<i>S. cerevisiae</i>	<i>B. taurus</i>
F₁ head		
α	α/Atp1	α
β	β/Atp2	β
F_o head		
γ	γ/Atp3	γ
δ	δ/Atp16	δ
ε	ε/Atp15	ε
Peripheral stalk		
b	b/Atp4	b
d	d/Atp7	d
F ₆	h/Atp14	F ₆
OSCP	OSCP/Atp5	OSCP
F_o motor		
a	a/Atp6	a
c	c/Atp9	c
Type I dimer-specific subunits		
e	e/Atp21	e
f	f/Atp17	f
g	g/Atp20	g
-	i/j/Atp18	6.8PL/ j
-	k/Atp19	DAPIT/ k
-	8/Atp8	A6L/ATP8

834 Nomenclature for yeast and mammalian species are described as detailed by Song and Pfanner
835 (6).

836 **Table S2. Metrics to assess confidence and fit of AlphaFold predicted structures**

Subunit name	<i>C. elegans</i> Uniprot Accession Number	Mean pLDDT (or weighted pTM & ipTM) ¹	RMSD between pruned atom pairs ²	RMSD across all atom pairs	Sequence alignment score ³
α	Q9XXK1	92.9066444	0.929	2.275	1869.6
β	P46561	87.5983733	1.241	2.961	1875.8
γ	Q95XJ0	92.17635904	0.914	2.058	665.4
δ	Q09544	85.82596715	0.901	2.488	224.7
ε ⁴	O16298	65.4116052			
	P34539	71.51756013	0.541	15.704	18.9
c	Q9BKS0	95.27668763	0.74	0.74	262.1
e	Q21732	89.96603434	0.993	10.078	79.8
f	Q22021	87.12810426	1.36	14.559	50.4
g	Q18803	90.2590889	1.318	10.538	112.8
a	P24888	77.54888203	1.154	4.824	308.5
b	Q20053	84.43326886			
	Q19126	84.74422485	1.004	15.512	332.8
d	Q17763	82.60642993	1.342	9.967	116.7
F ₆	O16517	89.9038886	0.992	15.452	43
OSCP	P91283	76.95722866	1.035	7.553	346.3
	Q7JNG1	76.43462181			
b,d,F ₆ multimer	Q19126, Q17763, O16517	0.712090029	1.324	11.335	327.9

¹ pLDDT scores are shown for subunits where structure was predicted individually, a weighted pTM and ipTM score is shown for a complex of subunits predicted using AlphaFold multimer. The pLDDT score is a per-residue measure of local confidence on a scale from 0 – 100. The predicted-TM score (pTM) and interface predicted-TM score (ipTM), and has a scale from 0-1.

² RMSD (Root Mean Square Deviation) is a measure of the similarity between two superimposed atomic coordinates, in this case for the predicted *C. elegans* subunits and the model of the *S. cerevisiae* ATP synthase dimer.

³ Sequence alignment score between *C. elegans* and *S. cerevisiae*.

⁴ Where a subunit has more than one isoform, the version with the highest pLDDT score was used to build the homology model. RMSD and sequence alignment scores are only shown for the selected protein. In the case of subunit b, the isoform with the highest pLDDT score is also the only isoform expressed in somatic tissues (70).

837 **Table S3. Metrics to assess fit of atomic detail models to *C. elegans* ATP synthase dimer**
838 **sub-tomogram averaging map.**

	<i>S. cerevisiae</i> atomic model [PDB 6B8H]	Original ⁵ <i>C. elegans</i> homology model	Adjusted ⁶ <i>C. elegans</i> homology model
PDB % atoms outside contour ⁷	14	15	6
MRC map ⁸ correlation score	0.8757	0.8643	0.9469

839

⁵ Homology model following scaffolding of AlphaFold predicted *C. elegans* subunits onto the *S. cerevisiae* atomic model without adjusting for dimer angle.

⁶ Homology model following fitting of dimer angle adjusted *C. elegans* ATP synthase monomers to the *C. elegans* ATP synthase sub-tomogram averaging map.

⁷ This value is given by Chimera when fitting a PDB model to a map using the "fit in map" command.

⁸ MRC map generated from PDB's using pdb2mrc command in EMAN2 (71). This metric shows level of correlation between pdb2mrc map and our sub-tomogram average at the same resolution (38.6 Å).

840 **Movie S1 (separate file).** Movie showing a 360° rotation about the y-axis of a single segmented
841 *C. elegans* mitochondrion from the upper panel of Fig. 3A. An image sequence of 100 PNG files
842 was collected in IMOD, and the sequence montaged into a 10fps AVI file in Image J (64).

843

844 **Movie S2 (separate file).** Movie showing a 360° rotation about the y-axis of a single segmented
845 *S. cerevisiae* mitochondrion from the lower panel of Fig. 3A. An image sequence of 100 PNG files
846 was collected in IMOD, and the sequence montaged into a 10fps AVI file in Image J (64).

847 **SI References**

- 848 6. J. Song, N. Pfanner, T. Becker, Assembling the mitochondrial ATP synthase. *Proc. Natl.*
849 *Acad. Sci. USA*. **115**, 2850–2852 (2018).
- 850 11. K. M. Davies, C. Anselmi, I. Wittig, J. D. Faraldo-Gómez, W. Kühlbrandt, Structure of the
851 yeast F₁F_o-ATP synthase dimer and its role in shaping the mitochondrial cristae. *Proc.*
852 *Natl. Acad. Sci. USA*. **109**, 13602–13607 (2012).
- 853 30. H. Guo, S. A. Bueler, J. L. Rubinstein, Atomic model for the dimeric F_o region of
854 mitochondrial ATP synthase. *Science*. **358**, 936–940 (2017).
- 855 41. J. Jumper, *et al.*, Highly accurate protein structure prediction with AlphaFold. *Nature* **596**,
856 583–589 (2021).
- 857 47. F. Sievers, *et al.*, Fast, scalable generation of high-quality protein multiple sequence
858 alignments using Clustal Omega. *Mol. Syst. Biol.* **7**, 539 (2011).
- 859 48. M. Goujon, *et al.*, A new bioinformatics analysis tools framework at EMBL-EBI. *Nucleic*
860 *Acids Res.* **38**, W695–W699 (2010).
- 861 49. H. McWilliam, *et al.*, Analysis Tool Web Services from the EMBL-EBI. *Nucleic Acids Res.*
862 **41**, W597–W600 (2013).
- 863 50. R. Evans, *et al.*, Protein complex prediction with AlphaFold-Multimer. *bioRxiv* (2021)
864 <https://doi.org/10.1101/2021.10.04.463034> (November 30, 2021).
- 865 64. C. A. Schneider, W. S. Rasband, K. W. Eliceiri, NIH Image to ImageJ: 25 years of image
866 analysis. *Nat. Methods* **9**, 671–675 (2012).
- 867 67. Y. Fukasawa, *et al.*, MitoFates: Improved Prediction of Mitochondrial Targeting Sequences
868 and Their Cleavage Sites. *Mol. Cell. Proteomics* **14**, 1113–1126 (2015).
- 869 68. J. J. A. Armenteros, *et al.*, Detecting sequence signals in targeting peptides using deep
870 learning. *Life Sci. Alliance* **2**, e201900429 (2019).

- 871 70. I. Kawasaki, *et al.*, ASB-1, a germline-specific isoform of mitochondrial ATP synthase b
872 subunit, is required to maintain the rate of germline development in *Caenorhabditis*
873 *elegans*. *Mech. Dev.* **124**, 237–251 (2007).
- 874 71. G. Tang, *et al.*, EMAN2: An extensible image processing suite for electron microscopy. *J.*
875 *Struct. Biol.* **157**, 38–46 (2007)
- 876 72. A. P. Srivastava, *et al.*, High-resolution cryo-EM analysis of the yeast ATP synthase in a
877 lipid membrane. *Science* **360** (2018).
- 878 73. T. E. Spikes, Structural studies of the mitochondrial F-ATPase (doctoral thesis).
879 University of Cambridge. (2017) <https://doi.org/10.17863/CAM.21471> (December 7, 2022).
- 880 74. M. J. Runswick, *et al.*, The affinity purification and characterization of ATP synthase
881 complexes from mitochondria. *Open Biol.* **3** (2012).